Earth and Planetary Science Letters 416 (2015) 109–120

Contents lists available at ScienceDirect

Earth and Planetary Science Letters

www.elsevier.com/locate/epsl

Evidence for geochemical terranes on Mercury: Global mapping of major elements with MESSENGER's X-Ray Spectrometer

Shoshana Z. Weider [a,*], Larry R. Nittler [a], Richard D. Starr [b], Ellen J. Crapster-Pregont [c,d], Patrick N. Peplowski [e], Brett W. Denevi [e], James W. Head [f], Paul K. Byrne [a,g], Steven A. Hauck II [h], Denton S. Ebel [c,d], Sean C. Solomon [a,d]

[a] Department of Terrestrial Magnetism, Carnegie Institution of Washington, Washington, DC 20015, USA
[b] Physics Department, The Catholic University of America, Washington, DC 20064, USA
[c] Department of Earth and Planetary Sciences, American Museum of Natural History, New York, NY 10024, USA
[d] Lamont-Doherty Earth Observatory, Columbia University, Palisades, NY 10964, USA
[e] The Johns Hopkins University Applied Physics Laboratory, Laurel, MD 20723, USA
[f] Department of Earth, Environmental and Planetary Sciences, Brown University, Providence, RI 02912, USA
[g] Lunar and Planetary Institute, Universities Space Research Association, Houston, TX 77058, USA
[h] Department of Earth, Environmental, and Planetary Sciences, Case Western Reserve University, Cleveland, OH 44106, USA

ARTICLE INFO

Article history:
Received 29 September 2014
Received in revised form 5 January 2015
Accepted 21 January 2015
Editor: C. Sotin

Keywords:
Mercury
MESSENGER
X-ray fluorescence
spectroscopy
geochemistry

ABSTRACT

We have mapped the major-element composition of Mercury's surface from orbital MESSENGER X-Ray Spectrometer measurements. These maps constitute the first global-scale survey of the surface composition of a Solar System body conducted with the technique of planetary X-ray fluorescence. Full maps of Mg and Al, together with partial maps of S, Ca, and Fe, each relative to Si, reveal highly variable compositions (e.g., Mg/Si and Al/Si range over 0.1–0.8 and 0.1–0.4, respectively). The geochemical variations that we observe are consistent with those inferred from other MESSENGER geochemical remote sensing datasets, but they do not correlate well with units mapped previously from spectral reflectance or morphology. Location-dependent, rather than temporally evolving, partial melt sources were likely the major influence on the compositions of the magmas that produced different geochemical terranes. A large ($>5 \times 10^6$ km^2) region with the highest Mg/Si, Ca/Si, and S/Si ratios, as well as relatively thin crust, may be the site of an ancient and heavily degraded impact basin. The distinctive geochemical signature of this region could be the consequence of high-degree partial melting of a reservoir in a vertically heterogeneous mantle that was sampled primarily as a result of the impact event.

1. Introduction

Since the MErcury Surface, Space ENvironment, GEochemistry, and Ranging (MESSENGER) spacecraft (Solomon et al., 2001) was inserted into orbit around Mercury on 18 March 2011, its suite of instruments has been used to make measurements of the planet's surface composition. Mercury's ancient surface consists mostly of volcanic deposits that were likely produced by partial melting of the planet's mantle. The major-element composition of these rocks therefore provides important information on the behavior of the evolving mantle during Mercury's early history. The Mg and Al contents of surface materials are particularly good indicators of early differentiation and temporal evolution of partial melting processes at depth. Previous studies of MESSENGER datasets have shown that Mercury's surface is Mg- and S-rich, but Al-, Ca-, and Fe-poor compared with typical terrestrial and lunar crustal materials (e.g., Nittler et al., 2011; Evans et al., 2012), and that the planet has abundant levels of moderately volatile elements such as K (Peplowski et al., 2011, 2012) and Na (Peplowski et al., 2014). Considerable compositional heterogeneities across Mercury's surface have also been documented (Peplowski et al., 2012, 2014, 2015; Weider et al., 2012, 2014). The measured compositions indicate that Mercury's surface rocks are most similar to magnesian basalts (Stockstill-Cahill et al., 2012) and Fe-poor basaltic komatiites (Charlier et al., 2013).

Here we present global maps of the Mg/Si and Al/Si abundance ratios across Mercury's surface from data acquired by MESSENGER's X-Ray Spectrometer (XRS). These are the first global geochemical maps of Mercury, and indeed the first maps of global extent for any planetary body acquired via X-ray fluorescence (XRF).

* Corresponding author.
E-mail address: sweider@carnegiescience.edu (S.Z. Weider).

http://dx.doi.org/10.1016/j.epsl.2015.01.023
0012-821X/

Together with partial maps of S/Si, Ca/Si, and Fe/Si (Weider et al., 2014), these datasets provide a basis for investigating variations in major-element abundances across the surface of Mercury and their implications for the early history of the planet and its mantle evolution.

2. MESSENGER's X-Ray Spectrometer

The MESSENGER XRS consists of three planet-facing gas-proportional counter (GPC) detectors and a Sun-pointing Si-PIN detector within the Solar Assembly for X-rays (SAX) (Schlemm et al., 2007). All four detectors have an energy range of ~1–10 keV, but the energy resolution of the GPCs is insufficient to separate the fluorescent K_α lines of Mg, Al, and Si (at 1.25, 1.49, and 1.74 keV, respectively). A "balanced filter" approach (Starr et al., 2000) was therefore employed, in which thin foils of Mg and Al placed in front of two GPCs provide selective absorption at different energies and allow the fluorescent signals from these elements to be deconvolved (Adler et al., 1972; Trombka et al., 2000). The detector resolution at higher energies is sufficient to separate the characteristic fluorescence lines for elements at higher atomic number (Z) (i.e., S, Ca, Ti, and Fe).

XRS data integration periods vary with MESSENGER's location in its eccentric orbit. Integration times are shortest (to a minimum of 40 s) close to periapsis, which occurs over Mercury's high northern latitudes, and longest (up to 450 s) when the spacecraft is far from the planet. Collimators on the GPC detectors produce a hexagonal 12° field of view (FOV), which corresponds to a measurement "footprint" on the surface that varies in size from <100 km to >3000 km in effective diameter (Schlemm et al., 2007; Weider et al., 2012).

The X-ray spectra obtained by the GPC detectors can contain signals from a number of sources, which include: (i) background counts that arise from interactions between galactic cosmic rays or solar energetic particles and the detectors, (ii) characteristic fluorescent X-rays from the planet, (iii) solar X-rays scattered from the planet's surface, and (iv) episodic interactions between energetic electrons quasi-trapped in the planet's magnetosphere and the GPC detectors (e.g., Ho et al., 2012; Starr et al., 2012).

3. XRS data and analysis procedures

XRS measures characteristic XRF, induced by incident solar X-rays, from the top <100 μm of Mercury's surface. The XRS measurements are therefore sensitive to the highly variable solar X-ray flux (e.g., Bouwer, 1983). Characteristic XRF data can be obtained during two different phases of solar activity (see Fig. 1). During typical "quiet Sun" periods (i.e., when solar coronal plasma temperatures are less than ~8 MK), only XRF signals with energy less than ~2 keV (e.g., Mg, Al, and Si K_α lines) can be detected. During solar flare conditions, in contrast, heavier elements can be excited and produce measurable XRF. We generated element-ratio maps using a methodology (Weider et al., 2014) that combines XRF analyses with variable spatial resolution; see Section 5.

3.1. Flare data analysis

Previously published XRS results were based entirely on data obtained during solar flares. The flare analysis procedure we employed for this study follows Nittler et al. (2011) and Weider et al. (2012, 2014). Our forward modeling technique, based on the fundamental-parameters approach (e.g., Clark and Trombka, 1997; Nittler et al., 2001), is used to derive elemental abundances for Mercury's surface by fitting both the measured incident solar spectra and the planetary XRF spectra. The maps we present are derived from analyses of 731 individual measurements made during 457 solar flares (Table S1).

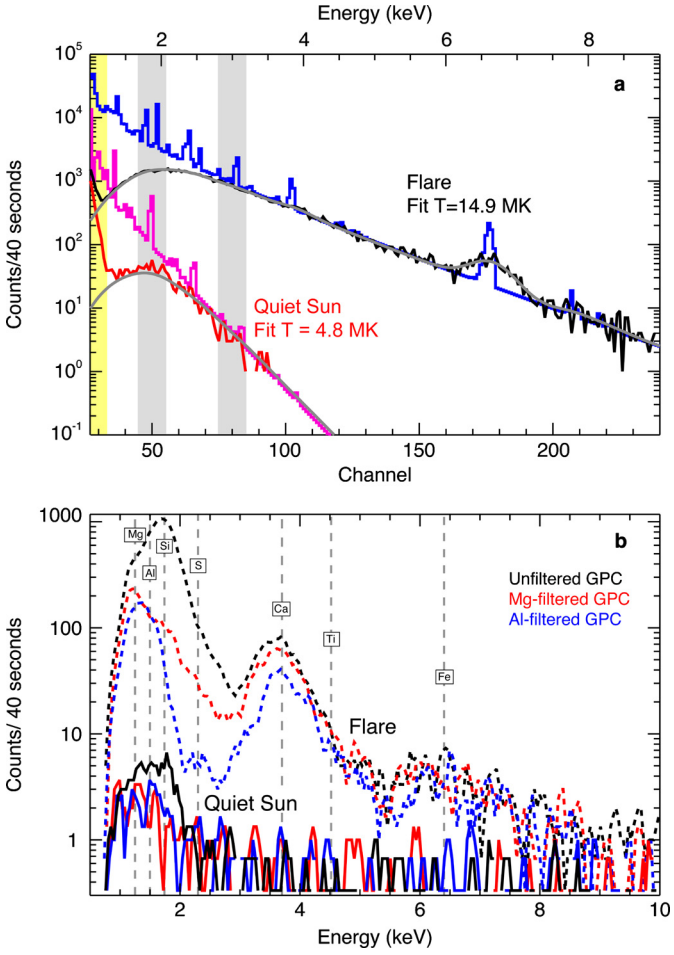

Fig. 1. Example MESSENGER XRS spectra (40 s integrations) from a solar flare (26 October 2013, 09:36 UTC) and a quiet-Sun period (18 October 2013, 01:21 UTC). (**a**) SAX solar spectra under flare (black) and quiet-Sun (red) conditions, and (**b**) the corresponding planetary XRF spectra from each GPC detector. Fits to the observed spectra in (**a**) are shown in grey, and the equivalent high-resolution solar flare spectra are shown in blue (flare) and pink (quiet Sun), along with the best-fit flare temperature (T). The yellow band indicates the spectral region dominated by electronic background. Grey bands show the channel ranges used to estimate the solar flare temperature for the quiet-Sun analysis (Section 3.2.3). Backgrounds have not been subtracted from the flare (dashed lines) and quiet-Sun (solid lines) spectra in (**b**). During flares, fluorescence from elements up to Fe is observed; during typical quiet-Sun periods fluorescence from only Mg, Al, and Si is detected and the overall signal level is much lower.

3.2. Quiet-Sun data analysis

3.2.1. Matrix inversion

It is more difficult to fit XRS spectra obtained during quiet-Sun conditions than during flare periods, for two reasons. First, the absence of fluorescence from high-Z elements removes several constraints on the spectral fitting parameters. Second, the large number ($>10^5$) of quiet-Sun spectra obtained during the MESSENGER mission makes the individual least-squares fitting approach (employed for the flare spectra) impractical. We thus developed a matrix-inversion approach to analyze the XRS quiet-Sun data. A similar methodology was used for analysis of Apollo 15 and 16 lunar XRF data (e.g., Yin et al., 1993).

For this approach, we assumed that the summed count rates for the GPC spectral channels (25–55), which cover the energy range 1.0–2.2 keV, are the result of the detector backgrounds plus the Mg, Al, and Si K_α XRF lines convolved with the relevant detector response at each energy:

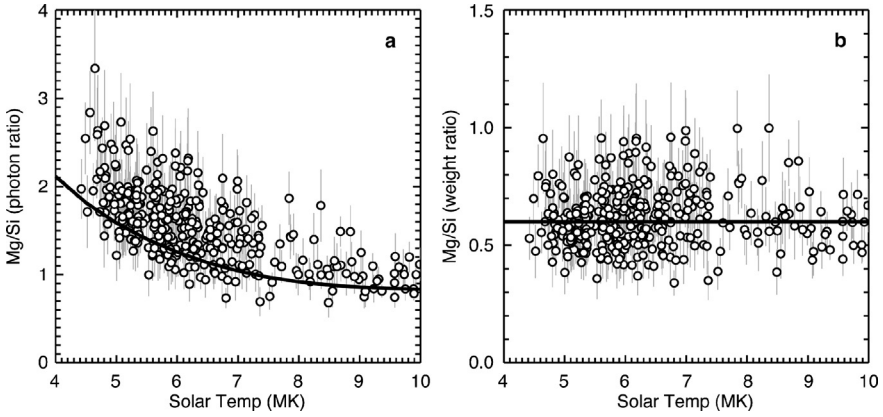

Fig. 2. (**a**) Mg/Si photon ratios derived from Eq. (1) for 362 quiet-Sun measurements, plotted as a function of estimated solar temperature (inferred with the SAX channel ratio method). These data come from measurements over large areas in Mercury's southern hemisphere and likely provide a representative average surface composition. The black curve indicates the predicted trend for a standard Mg/Si abundance ratio of 0.5. (**b**) Inferred Mg/Si elemental ratios on Mercury's surface for the data shown in (**a**). The fit (black line) to the data in (**b**) is flat, which indicates that the shape of the theoretical function relating Mg/Si photon ratio to solar temperature in (**a**) is accurate.

$$\begin{bmatrix} \varepsilon_{\mathrm{Mg},1} & \varepsilon_{\mathrm{Al},1} & \varepsilon_{\mathrm{Si},1} \\ \varepsilon_{\mathrm{Mg},2} & \varepsilon_{\mathrm{Al},2} & \varepsilon_{\mathrm{Si},2} \\ \varepsilon_{\mathrm{Mg},3} & \varepsilon_{\mathrm{Al},3} & \varepsilon_{\mathrm{Si},3} \end{bmatrix} \times \begin{bmatrix} \mathrm{Mg} \\ \mathrm{Al} \\ \mathrm{Si} \end{bmatrix} = \begin{bmatrix} C_1 \\ C_2 \\ C_3 \end{bmatrix} \quad (1)$$

where C_j is the observed (background-subtracted) count rate in detector j (1 = Mg-filtered GPC, 2 = Al-filtered GPC, 3 = unfiltered GPC); $\varepsilon_{i,j}$ is the jth detector response to the K_α line of element i; and Mg, Al, and Si are the K_α photon count rates of these elements incident on the XRS. Given the known ε-matrix (Table S2) and measured C_j values, we may invert Eq. (1) for the elemental XRF fluxes incident on the detectors. We used a least-squares approach to make accurate estimations (including background-subtraction error propagation). To relate the derived photon fluxes to surface elemental composition, a subsequent step is required (see Section 3.2.4).

3.2.2. Detector backgrounds

With our approach to the quiet-Sun analysis, it is necessary to treat effectively both the relatively low signal-to-background ratio and the variable GPC detector background levels. The GPC background levels can vary substantially (tens of percent) over timescales of hours or days. We therefore generated a database of GPC background count rates for our data analysis period to apply accurate background corrections and to propagate uncertainty for the quiet-Sun dataset. We manually examined the background count rates (measured when the instrument FOV does not include the planet) for each (Earth) day of the orbital mission, and we defined time intervals with relatively constant backgrounds. For each of these intervals we recorded the start and end times, as well as the mean count rates in each detector (and their standard deviations), summed over spectral channels 25–55 (see Fig. S1). These data provide the appropriate background correction and uncertainty in an accessible manner for any given XRS spectral integration.

3.2.3. Fitting solar spectra

As with flare analyses, converting the measured XRF fluxes into elemental abundance information requires knowledge of the incident solar spectra. The Be window in front of the SAX Si-PIN detector creates a steep drop-off in detector efficiency with decreasing energy (at energies less than ~2 keV). This drop-off makes accurate fitting of quiet-Sun SAX spectra difficult. Example SAX spectra from solar flare and quiet-Sun periods are shown in Fig. 1a, together with their lines of best fit and equivalent high-resolution theoretical solar spectra (generated with the *CHIANTI* code; Dere et al., 1997) that are used as inputs for the XRF modeling. The flare spectrum is easily fit because it exhibits high count rates that extend to high energies. The quiet-Sun spectrum, however, has much lower intensity and extends over a limited spectral range. The solar spectra used as inputs to the XRF modeling for quiet-Sun periods therefore involve substantial extrapolation from the observed data.

Because of the difficulty of fitting quiet-Sun SAX spectra, as well as the need to efficiently analyze the large SAX spectra database, we developed a simplified method to make accurate temperature estimates from quiet-Sun solar spectra. X-ray spectra emitted from hotter solar plasmas have higher overall intensities and are "harder" (i.e., decrease more slowly with increasing energy) than spectra from cooler plasmas (Fig. 1a). We make use of the SAX channel ratio (SCR), defined as the ratio of the sum of counts in channels 75–85 (equivalent to energies of ~2.8–3.2 keV) to that in channels 45–55 (equivalent to energies of ~1.7–2.1 keV). The flare and quiet-Sun spectra shown in Fig. 1a have SCRs of 0.58 and 0.08, respectively. We manually fit ~15,000 SAX (mostly quiet-Sun) spectra acquired during the first 22 months of MESSENGER's orbital observations and calculated the SCR for each spectrum. We subsequently determined a quadratic relationship between the SCR and solar plasma temperature:

$$T = 3.51 + 17.76(SCR) + 10.86(SCR)^2 \quad (2)$$

where T is the fit temperature in MK. We used this formula to relate the SCR to solar temperature for our quiet-Sun analyses (see Fig. S2); the estimated relative error in solar temperature inferred from this relation is 6%.

3.2.4. Estimation of elemental abundances

Mg/Si photon ratios, derived from Eq. (1), are shown in Fig. 2a as a function of solar temperature for 362 quiet-Sun spectra. These data constitute measurements over large areas in Mercury's southern hemisphere from random times during the first two years of MESSENGER's orbital mission. They thus likely provide a representative average surface composition. The measured Mg/Si photon ratios decrease with increasing solar temperature, as the solar X-ray spectrum hardens and induces more Si fluorescence relative to Mg. As with the XRS flare analyses, theoretical modeling of XRF and X-ray scattering is required to convert the measured detector signals (photon ratios in the quiet-Sun case) to elemental abundance information. To quantify quiet-Sun data, we therefore generated theoretical GPC spectra for a single assumed Mercury surface composition (for which Mg/Si = 0.5 and Al/Si = 0.23) that was based on previous XRS results (Nittler et al., 2001; Weider et al., 2012) for a range of solar coronal temperatures (3–15 MK). The theoretical spectra were calculated for a single assumed viewing geometry (45° incidence angle, 45° emission angle,

90° phase angle) and coronal elemental abundances typical of values derived during solar-flare spectral fitting.

We inverted the resultant synthetic spectra using Eq. (1) to predict Mg/Si and Al/Si photon ratios as functions of solar temperature (solid curve in Fig. 2a). Similar calculations for different assumed surface compositions indicate that Mg/Si and Al/Si photon ratios scale linearly with elemental ratios. We therefore used the derived curves (for Mg/Si and Al/Si) to convert the photon ratios to elemental ratios, i.e., for a given solar temperature the corresponding measured photon ratio is compared with the theoretical prediction, and abundance ratios are derived accordingly. The Mg/Si abundance ratios inferred from the data shown in Fig. 2a are plotted in Fig. 2b and show no residual temperature dependence, which indicates that the theoretical calibration curve accurately captures the functional shape.

The formal errors on the Mg/Si and Al/Si abundance ratios derived from single measurements with the matrix-inversion technique (e.g., those shown in Fig. 2b) are based on counting statistics and uncertainty in the detector backgrounds (see Section 3.2.2). Our method, however, is subject to other possible systematic uncertainties. For example, Eq. (1) is based on the assumption that only fluorescent Mg, Al, and Si X-rays are incident on the GPC detectors, whereas the actual planetary X-ray spectrum also includes a scattered solar continuum component. We largely correct for this inaccuracy because we derive calibration curves from synthetic GPC spectra that include the scattered solar component. Nevertheless, we tested the accuracy of our methodology in this respect. We used Eq. (1) to derive Mg/Si and Al/Si photon ratios for XRS flare spectra from which—with our flare analysis procedure—similar elemental abundance results were obtained. For those spectra with similar solar temperatures, the inferred relative photon ratios vary by ∼15% (an estimate of the intrinsic reproducibility for Mg/Si and Al/Si from the matrix-inversion analysis of a single XRS spectrum).

Additional uncertainties in the matrix-inversion approach may arise from (i) small changes in the detector energy calibrations, (ii) measurement viewing geometries different from those used in the calibration–curve generation, and (iii) varying abundances in the coronal plasmas from which the solar X-rays are emitted. We expect that these sources introduce small and random variations in the derived elemental abundance ratios. Variations caused by viewing geometry effects, in particular, have been the subject of several laboratory studies, which demonstrate that these effects are small for the closely spaced Mg, Al, and Si lines (e.g., Näränen et al., 2008; Weider et al., 2011). The maps we produce are based on averaging multiple measurements of the same area acquired at different times, so these random variations should be neutralized and should not contribute substantially to the final error budget. A more notable error is a systematic offset between abundance ratios derived via the matrix-inversion technique and those derived with our flare analysis procedure. We corrected empirically for this offset during the generation of our maps (see Section 5).

4. Data selection and binning

Our elemental abundance maps for Mg/Si and Al/Si are derived from both flare and quiet-Sun data (only flare data are used for the S/Si, Ca/Si, and Fe/Si maps) acquired between April 2011 and the end of December 2013. We searched the XRS database to find every solar flare period from which at least the Ca K_α line was observed, in addition to the solar flare data that have been presented previously (Nittler et al., 2011; Weider et al., 2012, 2014). We used our forward-modeling approach (see Section 3.1) to analyze all the flare data with measurement footprints in the northern hemisphere. We also analyzed the majority of data with footprints from the southern hemisphere, but excluded those flares with spectra that exhibited obvious contamination by charged particle interactions in the GPC detectors (i.e., Cu fluorescence from the instrument collimator and enhanced continuum at high energy).

Our initial quiet-Sun database included data with solar temperature estimates, derived from the SCR, of less than ∼10 MK. We selected all such data with footprints in the northern hemisphere and a random sampling of the data with footprints in the south. In addition, we included spectra from a few periods of higher flare temperature that had signal-to-noise ratios too low for reliable spectral fitting analysis. The dataset was filtered to exclude data (i) for which the count rate in the unfiltered GPC summed over channels 25–55 was <1–2 counts/s, since this number is the typical level of the detector background (Fig. S1); (ii) with excess signal at ∼8 keV (i.e., around the Cu K_α line, indicating charged-particle contamination in the detectors); and (iii) from the northern hemisphere with measurement footprints substantially larger than the typical XRS footprint for the same latitude.

The signal-to-noise ratios were sufficient in this preliminary dataset to permit reliable determination of Mg/Si for individual XRS spectral integrations, but not for Al/Si given the lower abundance of Al and the smaller dynamic range of Al/Si on Mercury's surface (Weider et al., 2012, 2014). We therefore performed spatial binning of the data prior to applying Eq. (1) and the conversion of the photon ratios to abundance ratios. We divided the planet into 3° × 3° bins and found all the data for measurements with center points in each bin. We then summed the GPC and SAX spectra for each bin and combined the data into a single spectrum for each detector (see Fig. S3). We used the summed GPC spectra to obtain detector count rates (Eq. (1)) and the summed SAX spectrum to estimate the solar temperature from the SCR (Eq. (2)). We applied the same spectral binning method for the Mg/Si and Al/Si maps so that they were derived from the same dataset and have the same spatial resolution.

We excluded additional data following the flare and quiet-Sun analyses. We removed data for which Mg/Si and/or Al/Si ratios were negative (indicating incorrect background subtraction) or with relative errors of >50% for the inferred Al/Si ratios. In addition, high Al/Si (and sometimes Mg/Si) ratios are thought to be caused by charged particle (especially electron) interactions with the Mg and Al foil filters on two of the GPCs. In many cases this contamination causes fluorescence of the XRS Cu collimator and creates excess counts in the spectra at high energy (∼8 keV). For many short northern-hemisphere integrations, however, the signal-to-noise ratio at these high energies is too low for detection of this signature. Our results indicate that essentially all measurements with Al/Si > 0.45, as well as those with Mg/Si > 0.63 and Al/Si > 0.3, exhibit some evidence of Cu fluorescence or are from regions with several other measurements that do not yield such high ratios. We assumed that all such measurements are contaminated and removed them from our final dataset. Finally, we excluded data that generated obvious outliers in one or more of the element ratios compared with other measurements from overlapping footprints. Our final maps were produced from 24,819 quiet-Sun analyses and 731 individual flare measurements; after binning, 4708 XRS footprints were combined to construct the maps.

5. Map generation

It is difficult to generate elemental ratio maps from XRS data because the spatial size of the measurement footprints changes substantially as a result of MESSENGER's eccentric orbit and changing periapsis altitude, and because of the highly variable solar X-ray output. Measurements with variable spatial resolution and statistical quality must therefore be combined. We used a recently developed method (Weider et al., 2014) to map the final XRS datasets. We divided the planet's surface into 0.25° × 0.25° pixels in a cylindrical projection. For a given elemental abundance ratio,

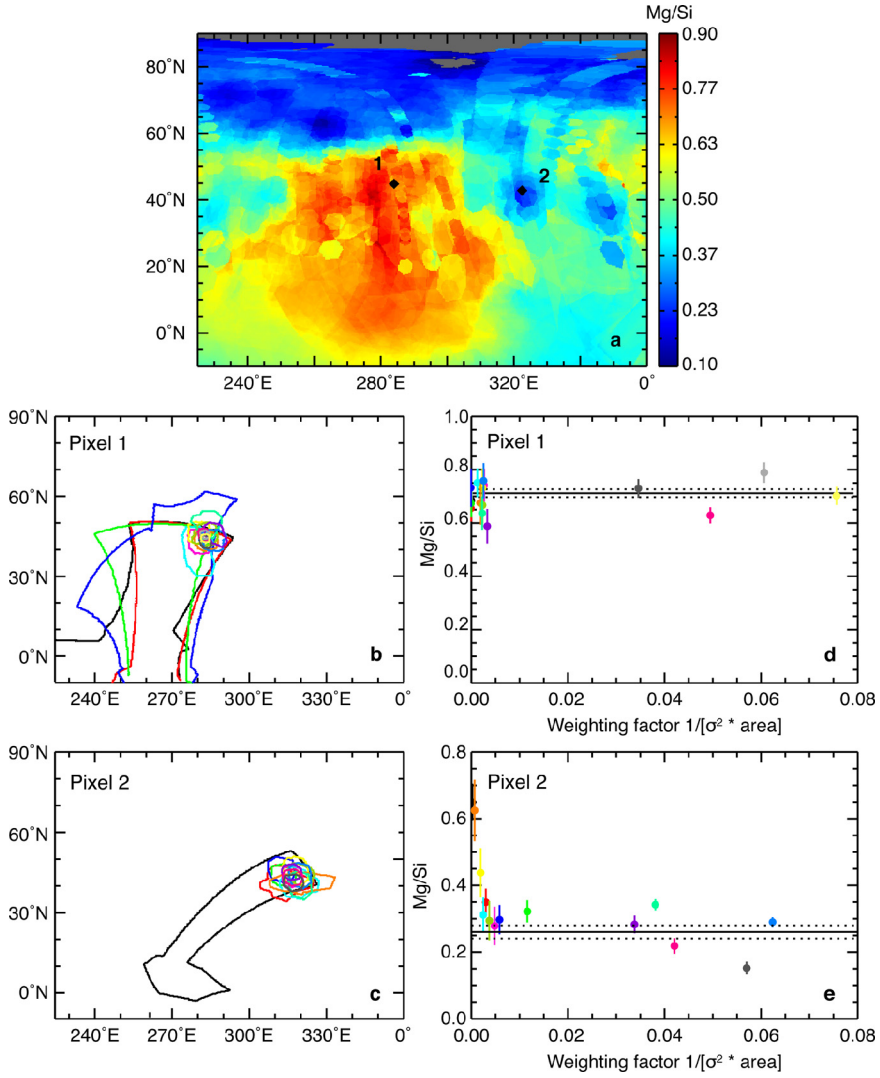

Fig. 3. Illustration of the XRS map generation procedure. (**a**) Portion of the full unsmoothed Mg/Si map (Fig. S5a), with two pixels labeled. (**b**) and (**c**) Outlines of the XRS footprints that overlap the two pixels. (**d**) and (**e**) Inferred Mg/Si ratios for each footprint plotted as a function of their weighting factor (Eq. (4)). Horizontal solid lines in (**d**) and (**e**) indicate the mean Mg/Si values derived from the data; dashed lines are ±1 standard deviation. The smallest footprints for each pixel have larger weighting factors and show reproducible results. Footprints with Mg/Si ratios that are substantially different from the mean pixel value are generally from larger footprints and thus incorporate other materials with different compositions.

R, each pixel is assigned a weighted mean R value from all the measurement footprints that overlap it:

$$R_{av} = \frac{\sum_{i=1}^{N} w_i R_i}{\sum_{i=1}^{N} w_i} \tag{3}$$

where N is the number of footprints overlapping a given pixel, and the weighting factor, w_i, is defined as:

$$w_i = \frac{1}{A_i \times \sigma_i^2} \tag{4}$$

where A_i is the surface area of the footprint and σ_i is the measurement error of R for footprint i. The mean pixel value is therefore weighted to favor (i) data from footprints with smaller areas, since they are more likely to represent a single geological unit on the surface, and (ii) measurements with smaller analytical errors. We define the uncertainty for a given pixel as a weighted standard error of the mean for the individual ratio measurements:

$$\sigma = \sqrt{\frac{\sum_{i=1}^{N} w_i (R_i - R_{av})^2}{(N-1)\sum_{i=1}^{N} w_i}} \tag{5}$$

When only a single XRS footprint overlaps a pixel, it is assigned the measured R value and an error that is based on the analytical uncertainty. The mapping procedure is illustrated in Fig. 3.

Our mapping approach is essentially a form of non-uniform image smoothing. To facilitate direct comparison of the XRS ratio maps with other information (e.g., surface reflectance), it is therefore necessary to smooth the other datasets in an identical way. To produce a comparable map of a quantity, Q, associated with single XRS footprints, we substitute Q_i values for R_i in Eq. (3) and use the weighting factors derived from the abundance ratio. For example, we derived "effective spatial resolution" maps by substituting the equivalent diameter of each flare footprint (assuming each footprint is circular) for R_i in Eq. (3).

For Mg/Si and Al/Si, we initially generated separate maps for flare analyses and quiet-Sun data. We expect flare data to be more accurate because the spectra have much higher signal-to-noise ratios and the derived abundances are based on spectral fitting. Furthermore, Mg/Si and Al/Si XRF ratios are much less sensitive to uncertainties in solar temperature estimates at flare temperatures than for quiet-Sun conditions. We thus assume that differences between the flare and quiet-Sun maps arise from systematic un-

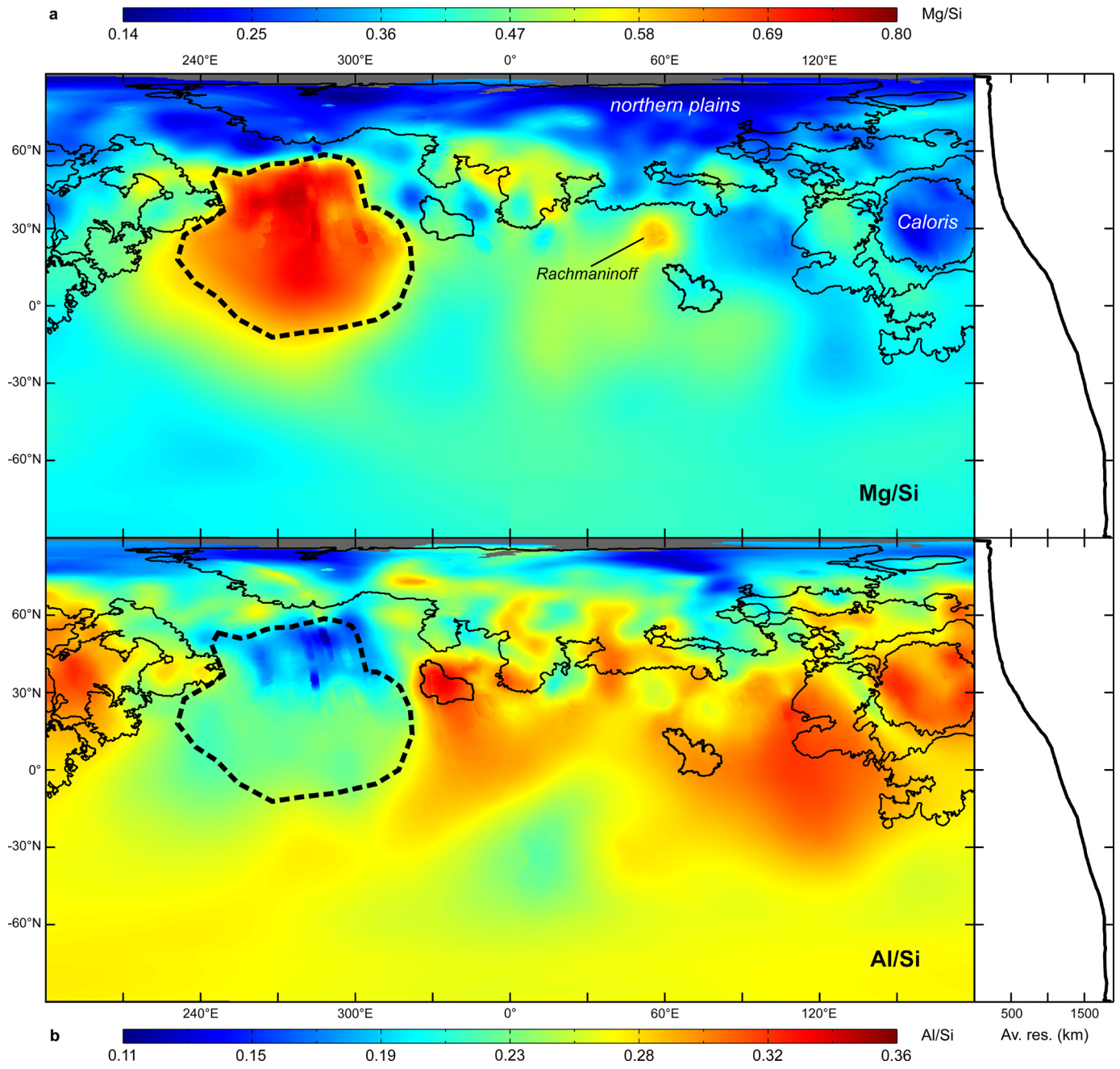

Fig. 4. Maps of (**a**) Mg/Si and (**b**) Al/Si (elemental weight ratios) derived from MESSENGER X-Ray Spectrometer measurements. Major deposits of smooth plains in the northern hemisphere, including those in the northern lowlands and those associated with the Caloris basin, are outlined by solid lines (Denevi et al., 2013). The Rachmaninoff impact basin is also labeled. The dashed line outlines the high-Mg region. Side panels illustrate the average spatial resolution of the measurements versus latitude.

certainties in the generation of the quiet-Sun map, and we accordingly apply empirical corrections.

Histograms of Mg/Si and Al/Si ratios from flare and quiet-Sun maps that include only pixels with both types of data (Fig. S4), illustrate offsets in the distribution of results. We multiplied the quiet-Sun data by empirically derived factors (0.828 for Mg/Si and 0.709 for Al/Si) to create scaled quiet-Sun distributions that are essentially identical to those for the flare data. The same factors were applied to all the quiet-Sun data, which were then combined with the flare measurements to create our maps. These factors correspond to a 20–30% systematic error in the quiet-Sun analysis, which is most likely a result of errors involved with fitting quiet-Sun SAX spectra to derive solar temperatures (see Section 3.2.3).

6. Results and discussion

6.1. Element ratio maps

Although our mapping procedure largely removes the outlines of individual footprints, some image artifacts remain at spatial scales less than the measurement resolution (Fig. S5). We therefore applied a second smoothing procedure, whereby the value of each pixel was replaced by the mean value of all the pixels surrounding it within a circular region of diameter equal to the effective resolution of the pixel, to create our final maps. Our global smoothed Mg/Si and Al/Si maps are shown in Fig. 4, and the smoothed S/Si, Ca/Si, and Fe/Si maps are shown in Fig. 5. Because of MESSENGER's eccentric orbit and high northern periapsis, the average spatial resolution of our maps varies with latitude (Fig. 4) and is best in the

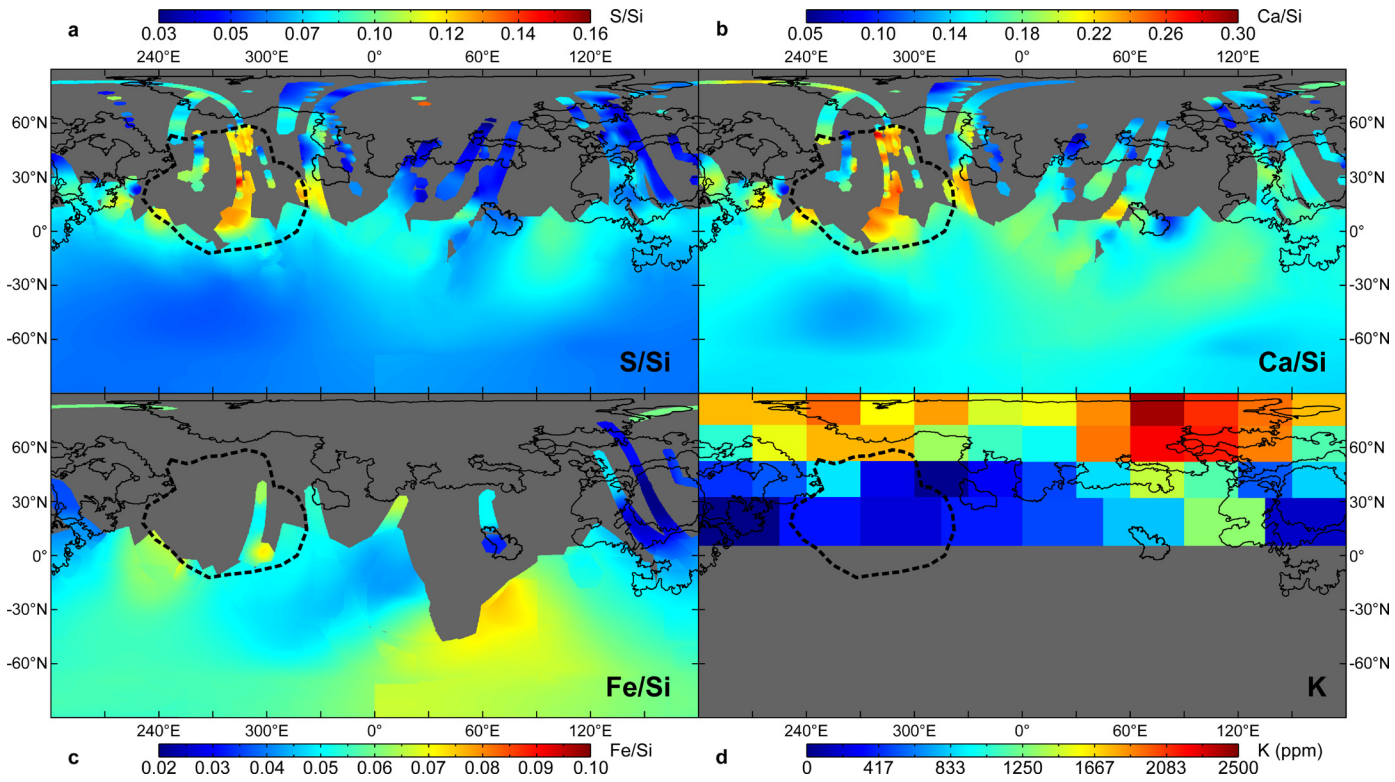

Fig. 5. Maps of (**a**) S/Si, (**b**) Ca/Si, and (**c**) Fe/Si (elemental weight ratios) derived from XRS measurements; and (**d**) K abundance derived from MESSENGER GRS data (Peplowski et al., 2012). Solid and dashed black lines are as in Fig. 4.

northern hemisphere. The Mg/Si and Al/Si maps have near-global coverage because they incorporate both quiet-Sun and solar flare analyses, whereas substantial gaps remain in the S/Si, Ca/Si, and Fe/Si maps, as these elements can be detected only during flares.

6.2. Mercury's geochemical terranes

The Mg/Si ratio of Mercury's surface (Fig. 4a) has a large dynamic range, varying by at least a factor of five. The Al/Si map (Fig. 4b) exhibits more variability on smaller spatial scales than the Mg/Si map, albeit with slightly larger analytical errors (Fig. S6). The lowest Mg/Si (∼0.1–0.2) ratios are found for the volcanic smooth plains (SP) within the Caloris impact basin and for parts of the northern plains (Head et al., 2011). Previous results (Weider et al., 2012), derived from more limited observations, showed a general compositional dichotomy, with the large expanse of SP within the northern lowlands having relatively low and uniform Mg/Si, as well as higher Al/Si, than the older, more heavily cratered terrain. Our complete maps, however, indicate that Mercury's geochemical diversity is more spatially complex.

The mean Mg/Si ratio of the northern plains is indeed lower than for the intercrater plains and heavily cratered terrain (ICP-HCT), but both Mg/Si and Al/Si vary by more than a factor of two within each of these regions. In addition, Mercury's heavily cratered terrain itself contains "geochemical terranes"—regions geochemically distinct from their surroundings—that have not been recognized before. The most obvious of these geochemical terranes is a large feature ($>5 \times 10^6$ km^2), centered at ∼30° N, 290° E, which exhibits the highest observed Mg/Si ratios (∼0.8). This high-magnesium region (HMR) also contains some of the lowest Al/Si ratios (Fig. 4b) on the planet's surface, as well as the highest S/Si (Fig. 5a) and Ca/Si (Fig. 5b) ratios. Fe/Si measurements from our dataset (Fig. 5c) provide only limited sampling of the HMR. It is difficult to estimate accurately the region's Fe content, but our results are consistent with the planetary average of ∼1.5–2 wt% Fe (Evans et al., 2012; Weider et al., 2014).

Some of the most distinct variations in composition seen in our global maps coincide with the boundaries of SP deposits (Denevi et al., 2013) that have been mapped on the basis of morphology and the size–frequency distribution of superposed impact craters. For instance, the Caloris interior smooth plains have lower Mg/Si and higher Al/Si than the surrounding geologic units. However, the compositional boundaries do not correspond precisely to the morphological and age boundaries of the northern plains in all locations (e.g., there is no compositional evidence for the northern plains boundary in the vicinity of 60–90° N, 240–270° E, and compositional changes around 30–60° N, 330–30° E do not coincide with the SP boundary). The highest observed Al/Si ratios (∼0.4) are confined to an SP deposit east of the HMR and south of the northern plains (∼35° N, 340° E), but this deposit has an intermediate Mg/Si ratio (∼0.5). No S, Ca, or Fe data are available for this region.

It is clear from our maps that the large expanse of northern plains does not have a single chemical composition, nor is it representative of Mercury's other major SP deposits. The northern low-Mg/Si area, however, has a similar spatial distribution to the high-K (>1500 ppm) region reported by Peplowski et al. (2012). We rebinned the XRS Mg/Si map to match the more coarse resolution of the K map, derived from MESSENGER Gamma-Ray Spectrometer (GRS) measurements (Fig. 5d), and found an inverse correlation between the two datasets (Fig. 6). A thermal redistribution scenario, under which K is mobilized from regions that experience higher than average surface temperatures to cooler parts of the planet, has previously been proposed to explain the mismatch between the surface distribution of K and the boundaries of the northern plains (Peplowski et al., 2012). It is difficult, however, to invoke redistribution of Mg (a non-volatile major element) through a similar mechanism. The inverse correlation between K and Mg/Si (Fig. 6) is therefore evidence against the thermal redistribution idea and

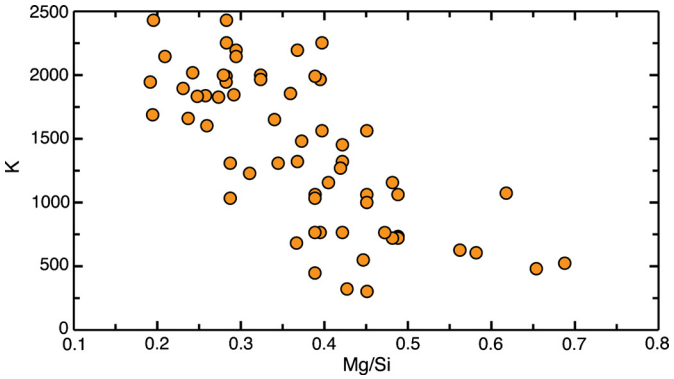

Fig. 6. Concentration of K (in ppm) (Peplowski et al., 2012) versus Mg/Si over Mercury's northern hemisphere. The Mg/Si dataset has been re-binned to match the spatial resolution of the GRS K measurements.

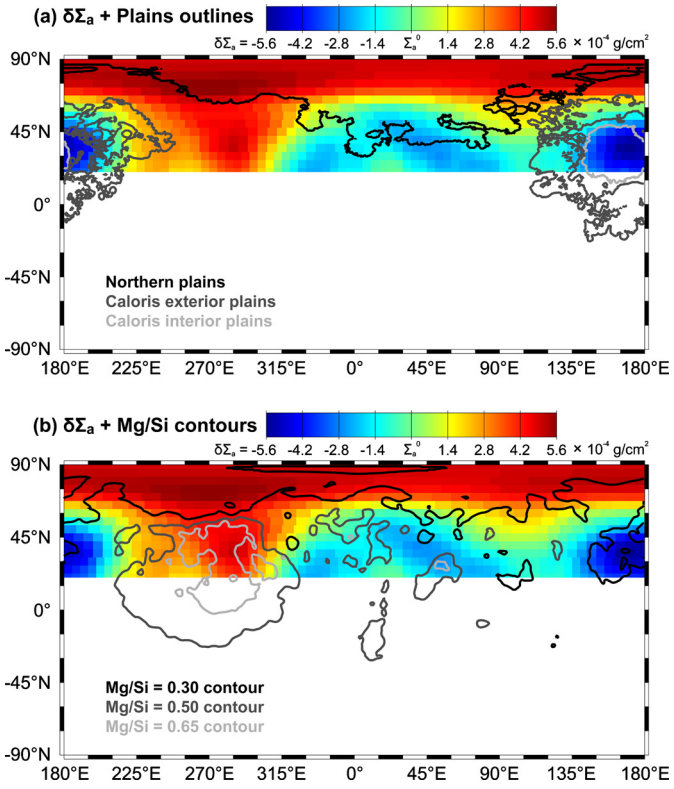

Fig. 7. Variability in macroscopic thermal neutron absorption ($\delta\Sigma_a$) across Mercury's northern hemisphere (Peplowski et al., 2015), about an arbitrary mean value (Σ_a^0). Outlines of mapped smooth plains units (Denevi et al., 2013) in (**a**) and XRS-derived Mg/Si abundance contours in (**b**) are shown for comparison. The lowest $\delta\Sigma_a$ values are spatially coincident with the Caloris interior smooth plains, a region that has distinct Mg/Si, Al/Si, and Fe/Si ratios (Figs. 4 and 5). Fe is an important neutron-absorbing element, and its low abundance in the Caloris interior plains is reflected in the low $\delta\Sigma_a$ values. The region of low Mg/Si in Mercury's high northern latitudes corresponds to a region with high $\delta\Sigma_a$ values. This correlation is likely due to elevated abundances of Cl (Evans et al., 2014) and Na (Peplowski et al., 2014, 2015) at these latitudes. The boundaries of this high $\delta\Sigma_a$ region, in agreement with the XRS measurements, do not match the geologically mapped boundaries of the northern plains unit (Denevi et al., 2013). The HMR also exhibits high $\delta\Sigma_a$ values, although the elements driving thermal neutron absorption in this region have yet to be identified (Peplowski et al., 2015).

instead supports spatial variations in the intrinsic composition of upper crustal material in this region.

A map of macroscopic neutron absorption (Fig. 7), derived from GRS thermal neutron measurements (Peplowski et al., 2015), reveals distinct geochemical units that are broadly compatible with those seen in the XRS data. Although the specific elements to

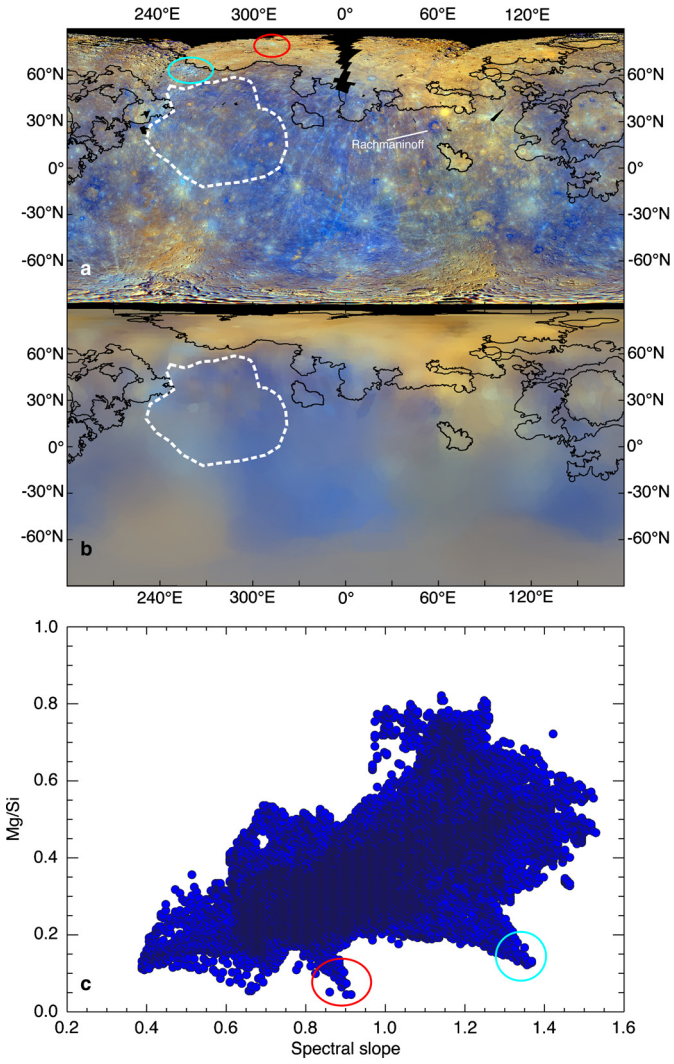

Fig. 8. (**a**) Enhanced color map constructed from MDIS wide-angle camera images. The red, green, and blue channels of the composite image are the second principal component, the first principal component, and the 430 nm/1020 nm reflectance ratio (spectral slope), respectively. (**b**) Enhanced color map, as in (**a**), smoothed to the effective resolution of the Mg/Si and Al/Si XRS maps (Fig. S5c). The major deposits of smooth plains in the northern hemisphere (outlined in black), the approximate outline of the HMR (dashed white line), and the Rachmaninoff basin are indicated. (**c**) Mg/Si ratio versus the blue channel (spectral slope, normalized to average value) of the smoothed enhanced color map for each of the map pixels. Red and cyan circles in (**a**) indicate regions with relatively fresh surfaces, which have color–composition trends that are distinct from the primary correlation seen in (**c**).

which the thermal neutron absorption map is sensitive vary spatially, the sensitivity for this measurement is largely dominated by variations in the abundances of Fe, as well as of the moderately volatile elements Na and Cl.

The spatial variations in composition we observe from the XRS data are also broadly consistent with changes in Mercury's surface spectral reflectance. We have compared the Mg/Si map with spectral reflectance properties of Mercury's surface, as defined by an "enhanced color" map (Fig. 8) derived from a principal component analysis of Mercury Dual Imaging System (MDIS) color images (e.g., Denevi et al., 2009). In the composite map (Fig. 8a), the red, green, and blue channels are the second principal component, first principal component, and ratio of reflectance at 430 nm to that at 1020 nm (a measure of spectral slope across visible and near-infrared wavelengths), respectively. Variations in the red–blue planes mainly highlight compositional differences, whereas the green channel is controlled mostly by surface maturity vari-

ations. The XRS Mg/Si map pixel values are plotted versus the corresponding value of the blue channel from the enhanced color map (normalized to its average value and smoothed to match the Mg/Si map, as described in Section 5 and shown in Fig. 8b) in Fig. 8c. There is a generally positive correlation between Mg/Si and spectral slope, but there is substantial scatter around the average trend, and some color–composition trends are distinct from the main correlation (e.g., circled regions in Fig. 8 that correspond to areas of fresh material with distinct color properties). Taken together, the maps of Mercury's surface composition suggest substantial variations that likely reflect variations in lithology, but such variations do not always match boundaries of previously mapped geological units.

On the basis of our maps, it is possible to define at least five geochemical terranes in addition to the HMR (see Fig. 9): (i) low-Mg northern SP, (ii) intermediate-Mg northern SP, (iii) Caloris interior SP, (iv) high-Al SP, and (v) the Rachmaninoff basin region. Many of these terranes show different correlations among element ratios (Fig. 9a). For instance, we observe separate Mg/Si–Al/Si trends for the HMR and the SP, which is in contrast to the findings of earlier work (Nittler et al., 2011; Weider et al., 2012; Charlier et al., 2013) that indicated two compositional end-members. The Mg/Si–Al/Si data are broadly consistent with a three-component distribution. Low-Fe basaltic komatiites or basalts are thought to be the best terrestrial analogues for Mercury's surface materials (Stockstill-Cahill et al., 2012; Charlier et al., 2013), i.e., Mercury's rocks are likely comprised mainly of Mg-rich orthopyroxene and olivine, as well as plagioclase feldspars (the probable dominant Al-bearing phase), on the basis of modeled mineralogies. With GRS data, it has been shown (Peplowski et al., 2014) that Mercury's surface has a relatively high Na content (>2.5 wt% Na), which is highest at the northernmost latitudes (~5 wt% Na versus ~2.6 wt% Na at more equatorial latitudes). The intermediate-Mg region of the northern plains (green in Fig. 9) also has a lower K content than the rest of the geologic unit (Fig. 5d). Different amounts of Na in the magmas that formed the distinct geochemical terranes would have affected the amount and type (anorthite or albite) of plagioclase produced (Charlier et al., 2013) and thereby the Al/Si ratios and Mg/Si–Al/Si trends seen in Fig. 9.

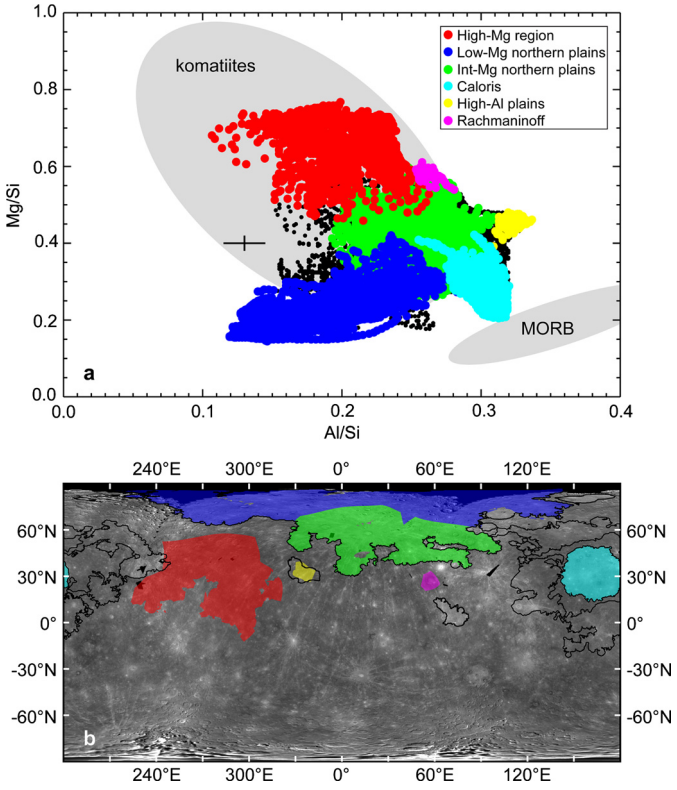

Fig. 9. (**a**) Mg/Si and Al/Si elemental ratios by weight for each 0.25° × 0.25° pixel in the global maps that has an effective spatial resolution smaller than 1000 km. Colored points indicate data from the specific regions shown in (**b**); red denotes the high-Mg region, blue the low-Mg northern smooth plains, green the intermediate-Mg northern smooth plains, cyan the Caloris interior smooth plains, yellow the high-Al smooth plains, and pink the Rachmaninoff region. Black points in (**a**) pertain to undefined regions, and grey fields indicate the compositions of terrestrial komatiites and mid-ocean ridge basalts (MORBs) (Weider et al., 2012). The cross in (**a**) denotes the median one-standard-deviation error in the data. Data points in (**a**) represent pixels with unequal areas in maps that have varying spatial resolution. The density of data points in (**a**) therefore does not correspond to their areal density on the planet.

6.3. Mantle heterogeneities and impact events

Charlier et al. (2013) showed (on the basis of more spatially limited XRS data; Nittler et al., 2011) that the variations in the composition of ICP-HCT on Mercury cannot be produced by fractional crystallization processes from a single magma source. Charlier et al. (2013) instead invoked partial melting of two different sources to account for the inferred compositional dichotomy (Nittler et al., 2011), i.e., the HMR and the surrounding ancient terrain of intermediate-Mg content are products of high-degree partial melting of a lherzolitic source and a harzburgitic source, respectively. The distinct sources may have formed from magma ocean crystallization and differentiation followed by decompression melting during mantle overturn or convection (Charlier et al., 2013). It has also been proposed that a decrease in the degree of mantle partial melting as the planet cooled over time could account for the overall lower Mg content of the northern plains compared with the older surrounding ICP-HCT (Weider et al., 2012).

The new maps clearly show, however, that such straightforward relationships cannot match the full range of observed compositional variations. A map of the areal density of impact craters at least 25 km in diameter (Marchi et al., 2013; Fig. 10a) indicates that the oldest (~4.1 Ga) and most heavily cratered parts of Mercury's surface exhibit the full range of Mg/Si ratios. Moreover, there are borders between older and younger units that do not display resolvable compositional variations (e.g., the northern plains boundary at ~75° N, ~240° E). Furthermore, the northern, circum-Caloris, and Caloris interior SP deposits have a limited range of crater densities (with estimated ages of ~3.6–3.8 Ga), but those units display considerable compositional heterogeneity. Given the shallow depth of Mercury's core–mantle boundary (Smith et al., 2012; Hauck et al., 2013), it is possible that mantle convection was not vigorous throughout the planet's evolution (Michel et al., 2013; Tosi et al., 2013) and therefore the mantle did not become well homogenized. Distinct magma sources (e.g., those proposed by Charlier et al., 2013) could therefore be distributed laterally, as well as vertically, within the mantle. As such, much of the variation in lava flow composition we observe could be a function of location-dependent mantle source conditions (e.g., composition, temperature, oxygen fugacity, depth). Impact-induced melting events are also likely to have influenced the location and character of Mercury's geochemical terranes.

The Rachmaninoff basin region (~28° N, ~303° E) is the most prominent area of high Mg/Si outside the HMR. The relatively young volcanic SP unit within the peak ring of this basin has reflectance characteristics that differ from those of the plains in the surrounding annular region of its floor (Prockter et al., 2010). The spectral properties of the annular plains—thought to have formed from impact melt—match those of low-reflectance material (LRM), a common spectral type on Mercury (Denevi et al., 2009). As discussed above, we observe a generally positive correlation between Mg/Si and spectral slope, i.e., the 430 nm/1020 nm

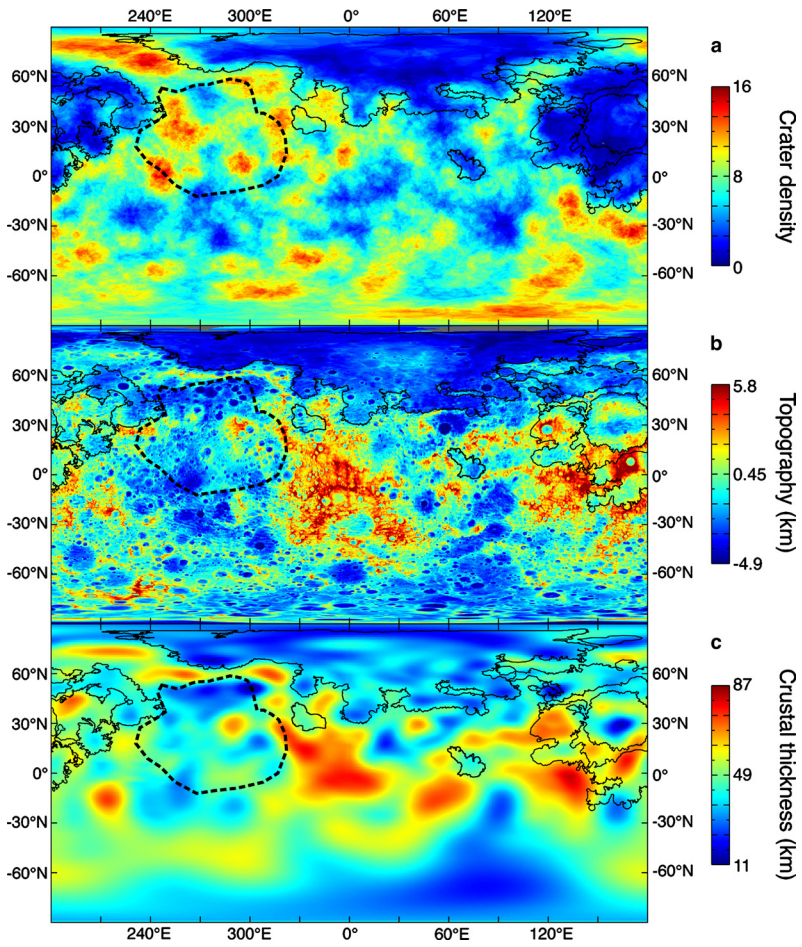

Fig. 10. Maps of **(a)** the areal density of impact craters, in number of craters at least 25 km in diameter per 10^5 km^2 (Marchi et al., 2013); (**b**) topographic elevation, relative to a sphere of radius 2440 km (Becker et al., 2012); and **(c)** crustal thickness (Smith et al., 2012). Major deposits of smooth plains in the northern hemisphere are outlined by solid black lines, and the dashed black line shows the approximate outline of the high-Mg region.

reflectance ratio (Fig. 8c). The source of LRM is thought to be heterogeneously distributed material from the lower crust or upper mantle that has likely been exposed at the surface by impact excavation (Denevi et al., 2009; Ernst et al., 2010; Rivera-Valentin and Barr, 2014). The strong LRM signature associated with Rachmaninoff (Fig. 8a), together with the high Mg/Si ratio, may be evidence of a Mg-rich magmatic body (Denevi et al., 2009) that was excavated during the basin-forming event. Sulfide minerals may be a key darkening phase on Mercury's surface (Blewett et al., 2013; Helbert et al., 2013) and therefore a component of LRM. Although there is not yet a spatially resolved S/Si measurement for the Rachmaninoff annular plains, the HMR (with a generally high 430 nm/1020 nm reflectance ratio) contains the highest S/Si ratios we have measured on the planet (Fig. 5a).

We suggest, therefore, that the HMR may also be an impact-related feature, and that its high Mg/Si ratio is evidence of mantle excavation during a large impact event early in Mercury's history (>4.1 Ga). Such a basin (defined by an ellipse of ~3700 km × 3000 km) would be over 1.5 times larger (in linear dimension) than Caloris, Mercury's largest well-preserved impact basin (e.g., Murchie et al., 2008). It would also be substantially larger than the Moon's South Pole–Aitken basin—about 2500 km in diameter (Spudis et al., 1994)—although smaller than the basin postulated to coincide with the northern lowlands of Mars (Marinova et al., 2008). The non-uniform crater density (see Fig. 10a) of the HMR indicates that, by this interpretation, the area must have been resurfaced at least partly by later volcanic activity.

6.4. High-Mg region: a giant impact basin?

If an ancient large impact at the HMR site penetrated into a vertically differentiated mantle (with additional lateral variations possible) and reached a deep, otherwise unsampled layer (i.e., the lherzolitic source proposed by Charlier et al., 2013), the HMR composition would be the signature of high-degree partial melting of that mantle source. The more recent and smaller Caloris impact may have penetrated only to shallower parts of a differentiated mantle (Roberts and Barnouin, 2012). Partial melting of previously depleted (e.g., in elements such as S) mantle sources—either by impact melting or earlier episodes of volcanism—in the Caloris region would have yielded a different chemical composition for the Caloris plains than for the HMR. Mantle heterogeneity combined with the effects of different size impact events occurring at different stages in Mercury's evolution can therefore account qualitatively for much of the surface compositional variation we have mapped. Furthermore, compositional variations that do not match the boundaries of the northern plains could be indicative of mantle sources for surface lavas that remained relatively uniform to produce the older intercrater plains as well as northern plains.

The HMR is characterized by generally low elevations (Fig. 10c) and thinner than average crust (Fig. 10b). These observations are consistent with the interpretation of the HMR as an ancient, heavily degraded impact basin. Although there is no obvious morphological evidence for such a basin structure (Fassett et al., 2012; Byrne et al., 2014), the HMR is an area with a paucity of confirmed large basins compared with other parts of Mercury's surface

of similar age (Marchi et al., 2013; Fassett et al., 2012). There is also an overall lack of basins with diameter > 500 km on Mercury compared with the Moon (Fassett et al., 2012). This difference has been attributed (Fassett et al., 2012) to (i) differences in the basin formation process on the two bodies, (ii) greater relaxation of topography after basin formation on Mercury, and/or (iii) higher rates of volcanism (which can fill, bury, and subdue impact basins) on Mercury during the period of basin formation. If Mercury's mantle had a higher average temperature than the lunar mantle during the period of heavy bombardment, these factors may have reinforced one another. By this reasoning, early impact basins that formed in a thin lithosphere would have experienced more efficient viscous relaxation (Mohit et al., 2009; Roberts and Barnouin, 2012) and lithospheric deformation (Klimczak et al., 2013), making it more difficult to recognize their diagnostic physiographic features (although the basin rim feature would still be difficult to destroy completely through relaxation and deformation processes).

7. Conclusions

Data from MESSENGER's X-Ray Spectrometer have yielded the first global geochemical maps of Mercury's surface. With a novel methodology, we have combined measurements obtained during solar flare and quiet-Sun periods to produce maps of Mg/Si and Al/Si elemental weight ratios. These maps are accompanied by less spatially complete maps of S/Si, Ca/Si, and Fe/Si that incorporate measurements from flare periods only. We have used these maps, together with other MESSENGER datasets, to study the geochemical characteristics of the planet's surface and to investigate the evolution of the mantle.

We find that Mercury's surface has substantial compositional variations and that its broad geochemical terranes do not always match previously mapped geologic units. The different compositions can be attributed to location-dependent source conditions (e.g., composition, temperature, oxygen fugacity, depth) of magma derived from a vertically and laterally heterogeneous mantle, coupled with the effects of large impact events. We propose that a large region with distinctively high Mg/Si, S/Si, Ca/Si, and low Al/Si ratios could represent high-degree partial melting of a mantle reservoir that had not previously undergone substantial depletion by melt extraction, but that was heated by an ancient large impact event.

The maps we have produced will be updated as the MESSENGER spacecraft and the XRS continue orbital operation at Mercury. New XRS data will have improved spatial resolution as the periapsis altitude of the spacecraft continues to decrease. These rich datasets will facilitate additional studies of Mercury's global-scale compositional variations, as well as smaller-scale studies focused on particular features of interest.

Acknowledgements

We gratefully acknowledge comments from Bernard Charlier and an anonymous reviewer on an earlier version of this paper. We thank the MESSENGER team for the highly successful operation of the MESSENGER spacecraft. This work is supported by the NASA Discovery Program under contract NAS5-97271 to The Johns Hopkins University Applied Physics Laboratory and NASW-00002 to the Carnegie Institution of Washington.

Appendix A. Supplementary material

Supplementary material related to this article can be found online at http://dx.doi.org/10.1016/j.epsl.2015.01.023.

References

Adler, I., Trombka, J., Gerard, J., Lowman, P., Schmadebeck, R., Blodget, H., Eller, E., Yin, L., Lamothe, R., Gorenstein, P., Bjorkholm, P., 1972. Apollo 15 geochemical X-ray fluorescence experiment: preliminary report. Science 175, 436–440.

Becker, K.J., Weller, L.A., Edmundson, K.L., Becker, T.L., Robinson, M.S., Enns, A.C., Solomon, S.C., 2012. Global controlled mosaic of Mercury from MESSENGER orbital images. Lunar Planet. Sci. 43. abstract 2654.

Blewett, D.T., Vaughan, W.M., Xiao, Z., Chabot, N.L., Denevi, B.W., Ernst, C.M., Helbert, J., D'Amore, M., Maturilli, A., Head, J.W., Solomon, S.C., 2013. Mercury's hollows: constraints on formation and composition from analysis of geological setting and spectral reflectance. J. Geophys. Res. Planets 118, 1013–1032. http://dx.doi.org/10.1029/2012JE004174.

Bouwer, S.D., 1983. Intermediate-term epochs in solar soft X-ray emission. J. Geophys. Res. 88, 7823–7830.

Byrne, P.K., Klimczak, C., Şengör, A.M.C., Solomon, S.C., Watters, T.R., Hauck II, S.A., 2014. Mercury's global contraction much greater than earlier estimates. Nat. Geosci. 7, 301–307.

Charlier, B., Grove, T.L., Zuber, M.T., 2013. Phase equilibria of ultramafic compositions on Mercury and the origin of the compositional dichotomy. Earth Planet. Sci. Lett. 363, 50–60.

Clark, P.E., Trombka, J.I., 1997. Remote X-ray spectrometry for NEAR and future missions: modeling and analyzing X-ray production from source to surface. J. Geophys. Res. 102, 16,361–16,384.

Denevi, B.W., Robinson, M.S., Solomon, S.C., Murchie, S.L., Blewett, D.T., Domingue, D.L., McCoy, T.J., Ernst, C.M., Head, J.W., Watters, T.R., Chabot, N.L., 2009. The evolution of Mercury's crust: a global perspective from MESSENGER. Science 324, 613–618.

Denevi, B.W., Ernst, C.M., Meyer, H.M., Robinson, M.S., Murchie, S.L., Whitten, J.L., Head, J.W., Watters, T.R., Solomon, S.C., Ostrach, L.R., Chapman, C.R., Byrne, P.K., Klimczak, C., Peplowski, P.N., 2013. The distribution and origin of smooth plains on Mercury. J. Geophys. Res. Planets 118, 891–907. http://dx.doi.org/10.1002/jgre.20075.

Dere, K.P., Landi, E., Mason, H.E., Monsignori Fossi, B.C., Young, P.R., 1997. CHIANTI – an atomic database for emission lines I. Wavelengths greater than 50 Å. Astron. Astrophys. Suppl. Ser. 125, 149–173.

Ernst, C.M., Murchie, S.L., Barnouin, O.S., Robinson, M.S., Denevi, B.W., Blewett, D.T., Head, J.W., Izenberg, N.R., Solomon, S.C., Roberts, J.H., 2010. Exposure of spectrally distinct material by impact craters on Mercury: implications for global stratigraphy. Icarus 209, 210–223.

Evans, L.G., Peplowski, P.N., Rhodes, E.A., Lawrence, D.J., McCoy, T.J., Nittler, L.R., Solomon, S.C., Sprague, A.L., Stockstill-Cahill, K.R., Starr, R.D., Weider, S.Z., Boynton, W.V., Hamara, D.K., Goldsten, J.O., 2012. Major-element abundances on the surface of Mercury: results from the MESSENGER Gamma-Ray Spectrometer. J. Geophys. Res. 117, E00L07. http://dx.doi.org/10.1029/2012JE004178.

Evans, L.G., Peplowski, P.N., Ebel, D.S., Lawrence, D.J., McCoy, T.J., Nittler, L.R., Starr, R.D., Weider, S.Z., Solomon, S.C., 2014. Chlorine on the surface of Mercury: implications for Mercury's surface evolution. Lunar Planet. Sci. 45. abstract 1794.

Fassett, C.I., Head, J.W., Baker, D.M.H., Zuber, M.T., Smith, D.E., Neumann, G.A., Solomon, S.C., Klimczak, C., Strom, R.G., Chapman, C.R., Prockter, L.M., Phillips, R.J., Oberst, J., Preusker, F., 2012. Large impact basins on Mercury: global distribution, characteristics, and modification history from MESSENGER orbital data. J. Geophys. Res. 117, E00L08. http://dx.doi.org/10.1029/2012JE004154.

Hauck II, S.A., Margot, J.-L., Solomon, S.C., Phillips, R.J., Johnson, C.L., Lemoine, F.G., Mazarico, E., McCoy, T.J., Padovan, S., Peale, S.J., Perry, M.E., Smith, D.E., Zuber, M.T., 2013. The curious case of Mercury's internal structure. J. Geophys. Res. Planets 118, 1204–1220. http://dx.doi.org/10.1002/jgre.20091.

Head, J.W., Chapman, C.R., Strom, R.G., Fassett, C.I., Denevi, B.W., Blewett, D.T., Ernst, C.M., Watters, T.R., Solomon, S.C., Murchie, S.L., Prockter, L.M., Chabot, N.L., Gillis-Davis, J.J., Whitten, J.L., Goudge, T.A., Baker, D.M.H., Hurwitz, D.M., Ostrach, L.R., Xiao, Z., Merline, W.J., Kerber, L., Dickson, J.L., Oberst, J., Byrne, P.K., Klimczak, C., Nittler, L.R., 2011. Flood volcanism in the northern high latitudes of Mercury revealed by MESSENGER. Science 333, 1853–1856.

Helbert, J., Maturilli, A., D'Amore, M., 2013. Visible and near-infrared reflectance spectra of thermally processed synthetic sulfides as a potential analog for the hollow forming materials on Mercury. Earth Planet. Sci. Lett. 369–370, 233–238.

Ho, G.C., Krimigis, S.M., Gold, R.E., Baker, D.N., Anderson, B.J., Korth, H., Slavin, J.A., McNutt Jr., R.L., Winslow, R.M., Solomon, S.C., 2012. Spatial distribution and spectral characteristics of energetic electrons in Mercury's magnetosphere. J. Geophys. Res. 117, A00M04. http://dx.doi.org/10.1029/2012JA017983.

Klimczak, C., Ernst, C.M., Byrne, P.K., Solomon, S.C., Watters, T.R., Murchie, S.L., Preusker, F., Balcerski, J.A., 2013. Insights into the subsurface structure of the Caloris basin, Mercury, from assessments of mechanical layering and changes in long-wavelength topography. J. Geophys. Res. Planets 118, 2030–2044. http://dx.doi.org/10.1002/jgre.20157.

Marchi, S., Chapman, C.R., Fassett, C.I., Head, J.W., Bottke, W.F., Strom, R.G., 2013. Global resurfacing of Mercury 4.0–4.1 billion years ago by heavy bombardment and volcanism. Nature 499, 59–61.

Marinova, M.M., Aharonson, O., Asphaug, E., 2008. Mega-impact formation of the Mars hemispheric dichotomy. Nature 453, 1216–1219.

Michel, N.C., Hauck II, S.A., Solomon, S.C., Phillips, R.J., Roberts, J.H., Zuber, M.T., 2013. Thermal evolution of Mercury as constrained by MESSENGER observations. J. Geophys. Res. Planets 118, 1033–1044. http://dx.doi.org/10.1002/jgre.20049.

Murchie, S.L., Watters, T.R., Robinson, M.S., Head, J.W., Strom, R.G., Chapman, C.R., Solomon, S.C., McClintock, W.E., Prockter, L.M., Domingue, D.L., Blewett, D.T., 2008. Geology of the Caloris basin, Mercury: a view from MESSENGER. Science 321, 73–76.

Mohit, P.S., Johnson, C.L., Barnouin-Jha, O., Zuber, M.T., Solomon, S.C., 2009. Shallow basins on Mercury: evidence of relaxation? Earth Planet. Sci. Lett. 285, 355–363.

Näränen, J., Parviainen, H., Muinonen, K., Carpenter, J., Nygård, K., Peura, M., 2008. Laboratory studies into the effect of regolith on planetary X-ray fluorescence spectroscopy. Icarus 198, 408–419.

Nittler, L.R., Starr, R.D., Lim, L., McCoy, T.J., Burbine, T.H., Reedy, R.C., Trombka, J.I., Gorenstein, P., Squyres, S.W., Boynton, W.V., McClanahan, T.P., Bhangoo, J.S., Clark, P.E., Murphy, M.E., Killen, R., 2001. X-ray fluorescence measurements of the surface elemental composition of asteroid 433 Eros. Meteorit. Planet. Sci. 36, 1673–1695.

Nittler, L.R., Starr, R.D., Weider, S.Z., McCoy, T.J., Boynton, W.V., Ebel, D.S., Ernst, C.M., Evans, L.G., Goldsten, J.O., Hamara, D.K., Lawrence, D.J., McNutt Jr., R.L., Schlemm II, C.E., Solomon, S.C., Sprague, A.L., 2011. The major-element composition of Mercury's surface from MESSENGER X-ray spectrometry. Science 333, 1847–1850.

Peplowski, P.N., Evans, L.G., Hauck II, S.A., McCoy, T.J., Boynton, W.V., Gillis-Davis, J.J., Ebel, D.S., Goldsten, J.O., Hamara, D.K., Lawrence, D.J., McNutt Jr., R.L., Nittler, L.R., Solomon, S.C., Rhodes, E.A., Sprague, A.L., Starr, R.D., Stockstill-Cahill, K.R., 2011. Radioactive elements on Mercury's surface from MESSENGER: implications for the planet's formation and evolution. Science 333, 1850–1852.

Peplowski, P.N., Lawrence, D.J., Rhodes, E.A., Sprague, A.L., McCoy, T.J., Denevi, B.W., Evans, L.G., Head, J.W., Nittler, L.R., Solomon, S.C., Stockstill-Cahill, K.R., Weider, S.Z., 2012. Variations in the abundances of potassium and thorium on the surface of Mercury: results from the MESSENGER Gamma-Ray Spectrometer. J. Geophys. Res. 117, E00L04. http://dx.doi.org/10.1029/2012JE004141.

Peplowski, P.N., Evans, L.G., Stockstill-Cahill, K.R., Lawrence, D.J., Goldsten, J.O., McCoy, T.J., Nittler, L.R., Solomon, S.C., Sprague, A.L., Starr, R.D., Weider, S.Z., 2014. Enhanced sodium abundance in Mercury's north polar region revealed by the MESSENGER Gamma-Ray Spectrometer. Icarus 228, 86–95.

Peplowski, P.N., Lawrence, D.J., Feldman, W.C., Goldsten, J.O., Bazell, D., Evans, L.G., Head, J.W., Nittler, L.R., Solomon, S.C., Weider, S.Z., 2015. Geochemical terranes of Mercury's northern hemisphere as revealed by MESSENGER neutron measurements. Icarus. http://dx.doi.org/10.1016/j.icarus.2015.02.002. In press.

Prockter, L.M., Ernst, C.M., Denevi, B.W., Chapman, C.R., Head III, J.W., Fassett, C.I., Merline, W.J., Solomon, S.C., Watters, T.R., Strom, R.G., Cremonese, G., Marchi, S., Massironi, M., 2010. Evidence for young volcanism on Mercury from the third MESSENGER flyby. Science 329, 668–671.

Rivera-Valentin, E.G., Barr, A.C., 2014. Impact-induced compositional variations on Mercury. Earth Planet. Sci. Lett. 391, 234–242.

Roberts, J.H., Barnouin, O.S., 2012. The effect of the Caloris impact on the mantle dynamics and volcanism of Mercury. J. Geophys. Res. 117, E02007. http://dx.doi.org/10.1029/2011JE003876.

Schlemm II, C.E., Starr, R.D., Ho, G.C., Bechtold, K.E., Hamilton, S.A., Boldt, J.D., Boynton, W.V, Bradley, W., Fraeman, M.E., Gold, R.E., Goldsten, J.O., Hayes, J.R., Jaskulek, S.E., Rossano, E., Rumpf, R.A., Schaefer, E.D., Strohbehn, K., Shelton, R.G., Thompson, R.E., Trombka, J.I., Williams, B.D., 2007. The X-Ray Spectrometer on the MESSENGER spacecraft. Space Sci. Rev. 131, 393–415.

Smith, D.E., Zuber, M.T., Phillips, R.J., Solomon, S.C., Hauck II, S.A., Lemoine, F.G., Mazarico, E., Neumann, G.A., Peale, S.J., Margot, J.-L., Johnson, C.L., Torrence, M.H., Perry, M.E., Rowlands, D.D., Goossens, S., Head, J.W., Taylor, A.H., 2012. Gravity field and internal structure of Mercury from MESSENGER. Science 336, 214–217.

Solomon, S.C., McNutt Jr., R.L., Gold, R.E., Acuña, M.H., Baker, D.N., Boynton, W.V., Chapman, C.R., Cheng, A.F., Gloeckler, G., Head III, J.W., Krimigis, S.M., McClintock, W.E., Murchie, S.L., Peale, S.J., Phillips, R.J., Robinson, M.S., Slavin, J.A., Smith, D.E., Strom, R.G., Trombka, J.I., Zuber, M.T., 2001. The MESSENGER mission to Mercury: scientific objectives and implementation. Planet. Space Sci. 49, 1445–1465.

Spudis, P.D., Reisse, R.A., Gillis, J.J., 1994. Ancient multiring basins on the Moon revealed by Clementine laser altimetry. Science 266, 1848–1851.

Starr, R., Clark, P.E., Murphy, M.E., Floyd, S.R., McClanahan, T.P., Nittler, L.R., Trombka, J.I., Evans, L.G., Boynton, W.V., Bailey, S.H., Bhangoo, J., Mikheeva, I., Brückner, J., Squyres, S.W., McCartney, E.M., Goldsten, J.O., McNutt Jr., R.L., 2000. Instrument calibrations and data analysis procedures for the NEAR X-Ray Spectrometer. Icarus 147, 498–519.

Starr, R.D., Schriver, D., Nittler, L.R., Weider, S.Z., Byrne, P.K., Ho, G.C., Rhodes, E.A., Schlemm II, C.E., Solomon, S.C., Trávníček, P., 2012. MESSENGER detection of electron-induced X-ray fluorescence from Mercury's surface. J. Geophys. Res. 117, E00L02. http://dx.doi.org/10.1029/2012JE004118.

Stockstill-Cahill, K.R., McCoy, T.J., Nittler, L.R., Weider, S.Z., Hauck II, S.A., 2012. Magnesium-rich crustal compositions on Mercury: implications for magmatism from petrologic modeling. J. Geophys. Res. 117, E00L15. http://dx.doi.org/10.1029/2012JE004140.

Tosi, N., Grott, M., Plesa, A.-C., Breuer, D., 2013. Thermochemical evolution of Mercury's interior. J. Geophys. Res. Planets 118, 2474–2487. http://dx.doi.org/10.1002/jgre.20168.

Trombka, J.I., Squyres, S.W., Brückner, J., Boynton, W.V., Reedy, R.C., McCoy, T.J., Gorenstein, P., Evans, L.G., Arnold, J.R., Starr, R.D., Nittler, L.R., Murphy, M.E., Mikheeva, I., McNutt Jr., R.L., McClanahan, T.P., McCartney, E., Goldsten, J.O., Gold, R.E., Floyd, S.R., Clark, P.E., Burbine, T.H., Bhangoo, J.S., Bailey, S.H., Petaev, M., 2000. The elemental composition of asteroid 433 Eros: results of the NEAR-Shoemaker X-ray spectrometer. Science 289, 2101–2105.

Weider, S.Z., Swinyard, B.M., Kellett, B.J., Howe, C.J., Joy, K.H., Crawford, I.A., Gow, J., Smith, D.R., 2011. Planetary X-ray fluorescence analogue laboratory experiments and an elemental abundance algorithm for C1XS. Planet. Space Sci. 59, 1393–1407.

Weider, S.Z., Nittler, L.R., Starr, R.D., McCoy, T.J., Stockstill-Cahill, K.R., Byrne, P.K., Denevi, B.W., Head, J.W., Solomon, S.C., 2012. Chemical heterogeneity on Mercury's surface revealed by the MESSENGER X-Ray Spectrometer. J. Geophys. Res. 117, E00L05. http://dx.doi.org/10.1029/2012JE004153.

Weider, S.Z., Nittler, L.R., Starr, R.D., McCoy, T.J., Solomon, S.C., 2014. Variations in the abundance of iron on Mercury's surface from MESSENGER X-Ray Spectrometer observations. Icarus 235, 170–186. http://dx.doi.org/10.1016/j.icarus.2014.03.002.

Yin, L.I., Trombka, J.I., Adler, I., Bielefeld, M., 1993. X-ray remote sensing techniques for geochemical analysis of planetary surfaces. In: Pieters, C.M., Englert, P.A. (Eds.), Remote Geochemical Analysis: Elemental and Mineralogical Composition. Cambridge University Press, Cambridge, UK, pp. 199–212.

Supporting materials for

Evidence for geochemical terranes on Mercury: Global mapping of major elements with MESSENGER's X-Ray Spectrometer

Shoshana Z. Weider, Larry R. Nittler, Richard D. Starr, Ellen J. Crapster-Pregont, Patrick N. Peplowski, Brett W. Denevi, James W. Head, Paul K. Byrne, Steven A. Hauck, II, Denton S. Ebel, Sean C. Solomon.

This file contains two supplementary tables (Table S1 is provided as an accompanying spreadsheet) and six supplementary figures, which illustrate aspects of the data selection, analysis, and mapping procedures.

Table S1. List of individual solar flare measurements, with which element-ratio maps (**Figs. 4 and 5**) were constructed.

(see accompanying Excel spreadsheet)

Notes: Derived solar temperatures and elemental ratios are given along with their uncertainties. Several spectra from consecutive integrations have been summed to derive the Fe/Si ratios (see Weider et al., 2014, for more details). Measurements that have previously been analyzed are indicated.

Table S2. Efficiencies of each GPC detector ($\varepsilon_{i,j}$) used in Eq. 1.

Detector	Mg K_α	Al K_α	Si K_α
1. Mg-filtered GPC	0.1426	0.0160	0.0601
2. Al-filtered GPC	0.0702	0.1885	0.0027
3. Unfiltered GPC	0.2110	0.3780	0.5250

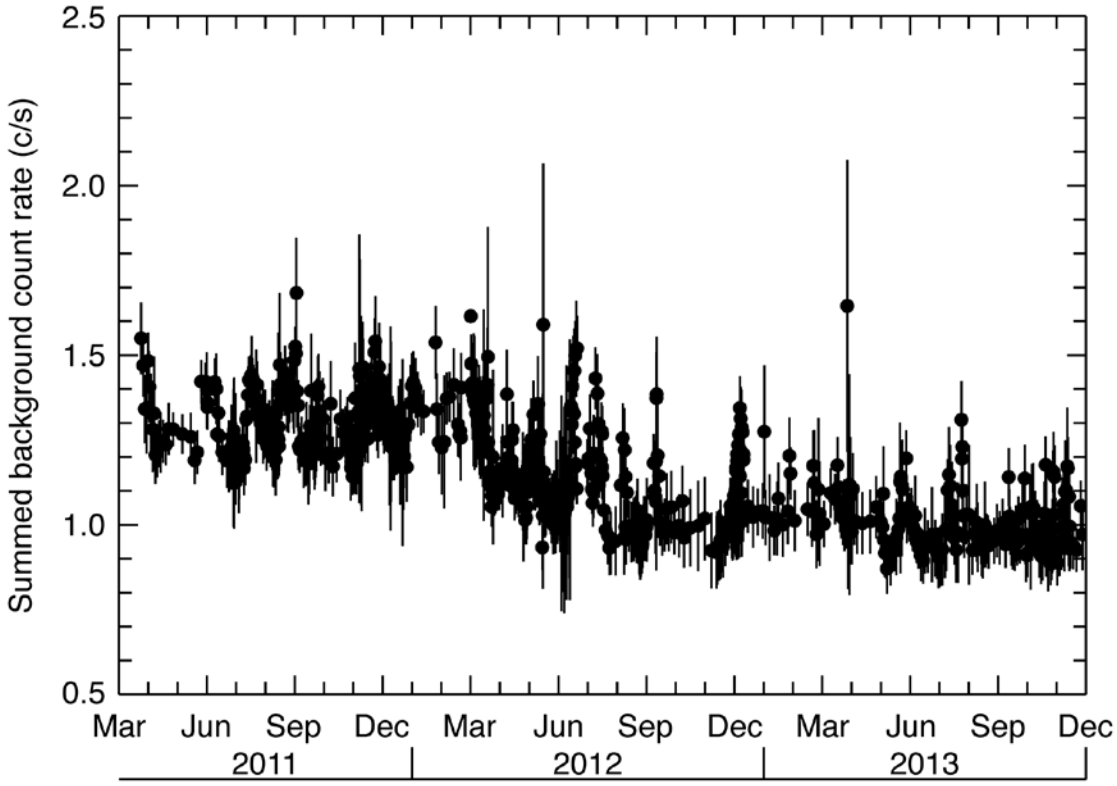

Fig. S1. Mean background count rates (in counts per second, or c/s) from the unfiltered GPC detector, summed over channels 25–55 (energy ~1.0–2.2 keV), for each Earth day from April 2011 through December 2013. Errors are one standard deviation. For comparison, the median XRF signal count rate in the unfiltered detector (for the data used to construct our maps) in the same channel range was ~7 c/s.

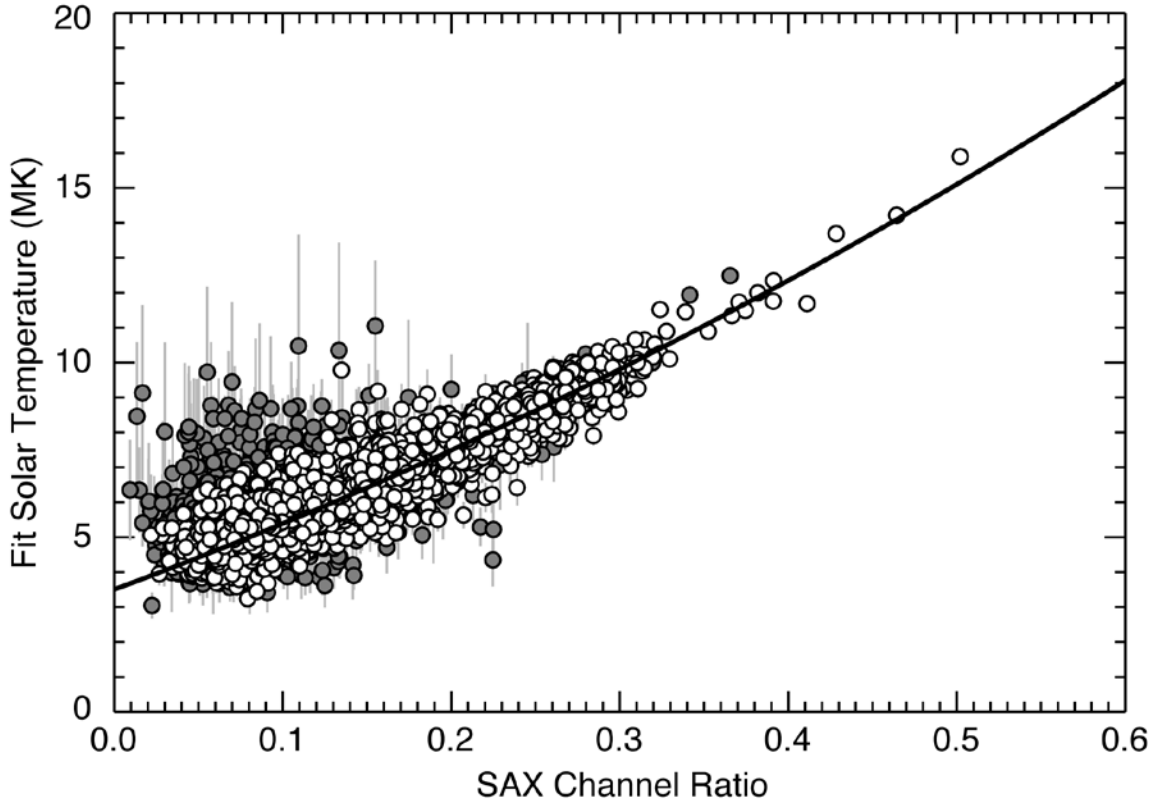

Fig. S2. Solar coronal temperature (in 10^6 K) derived from fitting ~15,000 SAX spectra versus SAX channel ratio (ratio of the summed counts in channels 75–85 to those in channels 45–55). White circles are for the ~10,000 spectra for which the error in the fit-derived temperature is <10%. The black curve shows a quadratic fit to these low-error data. The spread of data around the quadratic curve illustrates the ~6% relative uncertainty that is inherent to the SAX channel-ratio method of solar temperature estimation. Several of the spectra that plot away from the best-fit curve have poor spectral fits. The channel ratio is therefore a more reliable method of solar temperature estimation than spectral fitting for low signal-to-noise quiet-Sun SAX spectra.

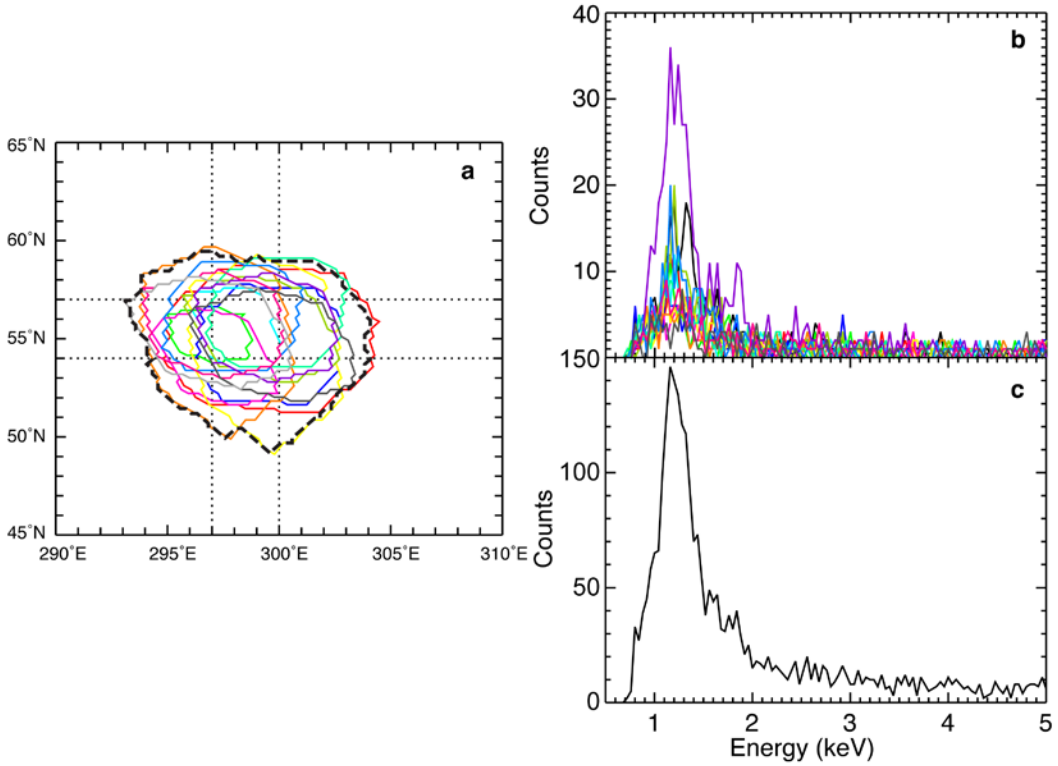

Fig. S3. Illustration of the spectral binning process. (**a**) Outlines of 14 individual quiet-Sun XRS measurement footprints. The center of these footprints is in the longitudinal and latitudinal range indicated by the dotted lines. The thick black dashed line represents the outline of the combined footprint. (**b**) Spectra from the Al-filtered GPC for each of the 14 measurements. (**c**) Summed spectrum. The summed spectrum has a much higher signal-to-noise ratio than any of the individual spectra.

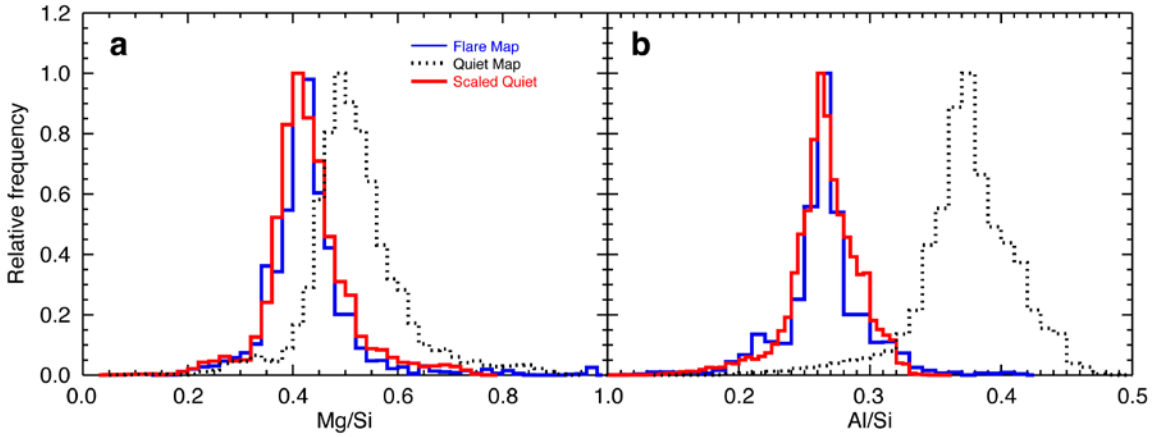

Fig. S4. Distribution of pixel data from the (**a**) Mg/Si and (**b**) Al/Si maps. Blue lines indicate data derived solely from flare data, and dotted black lines are results from quiet-Sun data. Empirically corrected quiet-Sun data (red) are scaled to match the flare distributions (see **section 5** for details).

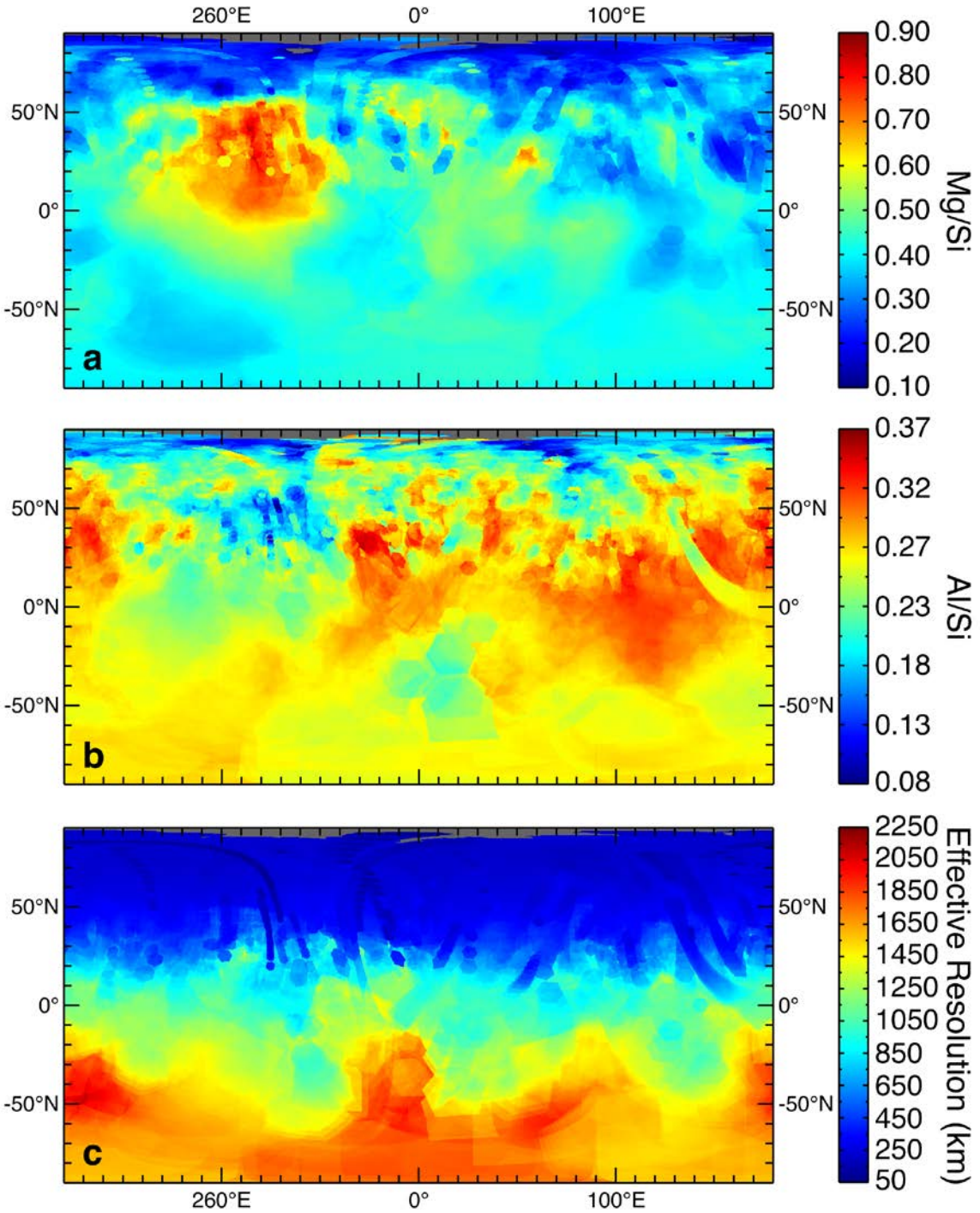

Fig. S5. Complete (flare plus quiet Sun) maps for (**a**) Mg/Si and (**b**) Al/Si. (**c**) Effective spatial resolution for both maps.

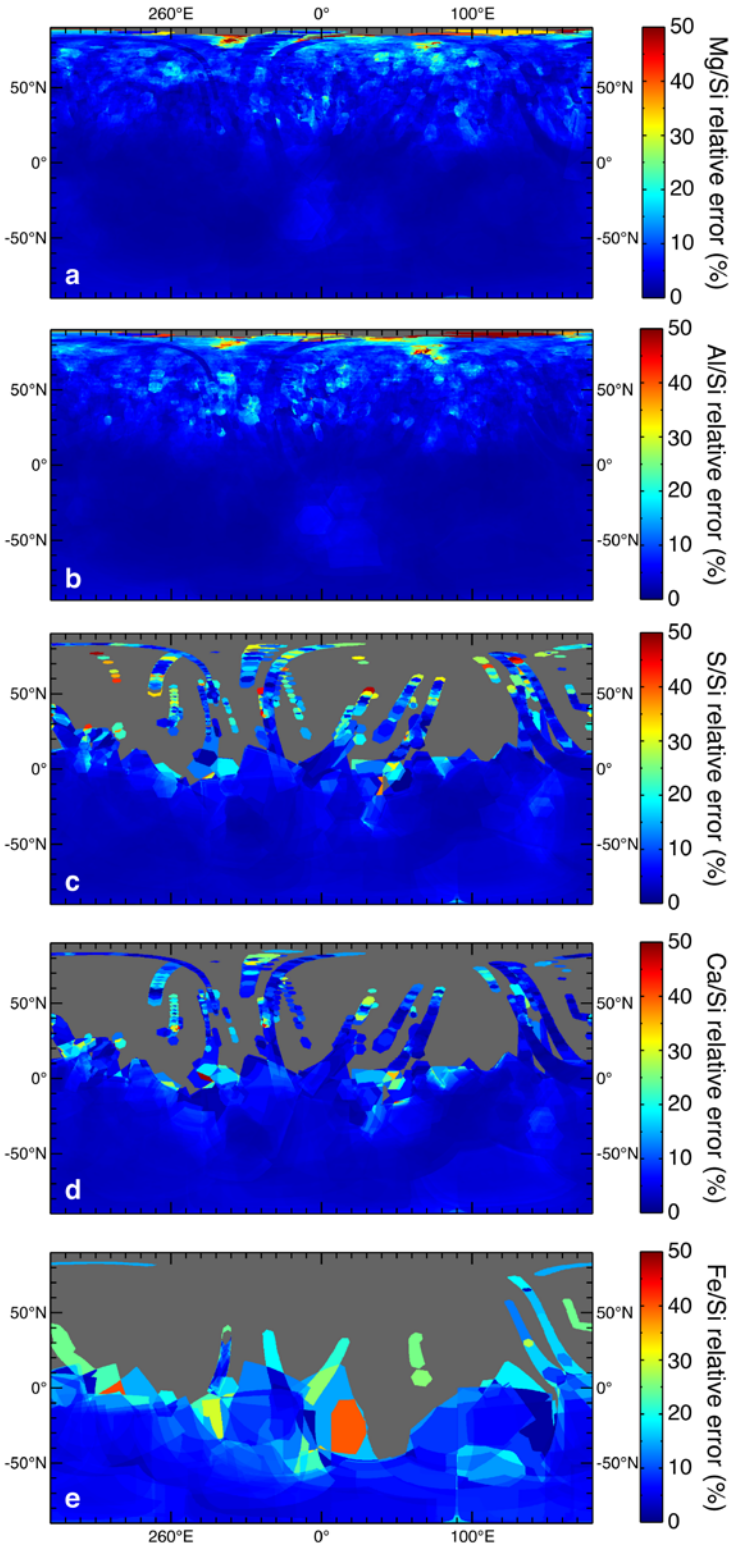

Fig. S6. Relative errors for the XRS-derived (**a**) Mg/Si, (**b**) Al/Si, (**c**) S/Si, (**d**) Ca/Si, and (**e**) Fe/Si maps (as shown in **Figs. 4 and 5**).